RWTH Aachen University
&
TU Bergakademie Freiberg

Master of Science Thesis in Applied Geophysics

Seismic depth imaging of sea-level controlled depositional sequences at the New Jersey shelf

Author:
Kira Asshoff

Supervisors:
Dr. Sönke Reiche
Prof. Dr. Stefan Buske

August 2016

Seismic depth imaging of sea-level controlled depositonal sequences at the New Jersey shelf

Master of Science Thesis

for the degree of Master of Science in Applied Geophysics at

Delft University of Technology

ETH Zürich

RWTH Aachen University

by

Kira Asshoff

August 12, 2016

Department of Geoscience & Engineering
Department of Earth Sciences
Faculty of Georesources and Material Engineering

Delft University of Technology
ETH Zürich
RWTH Aachen University

Printed in Germany

IDEA LEAGUE
JOINT MASTER'S IN APPLIED GEOPHYSICS

Delft University of Technology, The Netherlands
ETH Zürich, Switzerland
RWTH Aachen University, Germany

Dated: *August 12, 2016*

Supervisors:

Dr. S. Reiche

Prof. S. Buske

Committee Members:

Dr. S. Reiche

Prof. H. Maurer

Eidesstattliche Versicherung

Asshoff, Kira _____

Name, Vorname

_____

Matrikelnummer (freiwillige Angabe)

Ich versichere hiermit an Eides Statt, dass ich die vorliegende Arbeit/Bachelorarbeit/ Masterarbeit* mit dem Titel

Seismic depth imaging of sea-level controlled depositional sequences at the New Jersey shelf

selbständig und ohne unzulässige fremde Hilfe erbracht habe. Ich habe keine anderen als die angegebenen Quellen und Hilfsmittel benutzt. Für den Fall, dass die Arbeit zusätzlich auf einem Datenträger eingereicht wird, erkläre ich, dass die schriftliche und die elektronische Form vollständig übereinstimmen. Die Arbeit hat in gleicher oder ähnlicher Form noch keiner Prüfungsbehörde vorgelegen.

Paderborn, 10.08.2016 _____

Ort, Datum

Unterschrift

*Nichtzutreffendes bitte streichen

Belehrung:

§ 156 StGB: Falsche Versicherung an Eides Statt

Wer vor einer zur Abnahme einer Versicherung an Eides Statt zuständigen Behörde eine solche Versicherung falsch abgibt oder unter Berufung auf eine solche Versicherung falsch aussagt, wird mit Freiheitsstrafe bis zu drei Jahren oder mit Geldstrafe bestraft.

§ 161 StGB: Fahrlässiger Falscheid; fahrlässige falsche Versicherung an Eides Statt

(1) Wenn eine der in den §§ 154 bis 156 bezeichneten Handlungen aus Fahrlässigkeit begangen worden ist, so tritt Freiheitsstrafe bis zu einem Jahr oder Geldstrafe ein.

(2) Straflosigkeit tritt ein, wenn der Täter die falsche Angabe rechtzeitig berichtigt. Die Vorschriften des § 158 Abs. 2 und 3 gelten entsprechend.

Die vorstehende Belehrung habe ich zur Kenntnis genommen:

Paderborn, 10.08.2016 _____

Ort, Datum

Unterschrift

Abstract

This master thesis is part of a joint project carried out at TU Bergakademie Freiberg and RWTH Aachen University, aspiring to simulate numerically the fresh water emplacement and recharge system at the New Jersey shelf. Analyses of data, acquired during the most recent seismic drilling campaign IODP Leg 313 at the New Jersey shelf, revealed complex salinity variations with depth (Lofi et al., 2013). Additionally, fresh water reservoirs with a salinity lower than 3 g/L have been discovered down to 400 m depth below the seafloor and up to 130 km far-off the New Jersey coast (Mountain et al., 2010; Post et al., 2013). The origin of the freshwater distribution so far-off the New Jersey coast is still unknown, leading to an ongoing debate over two conflicting hypotheses. It is the main objective of the joint research, to achieve a better understanding of these vertical salinity variations and the controlling factors of groundwater circulation at the NJ shelf.

Re-processing and depth imaging of the available seismic data are necessary for deriving a reliable 3D subsurface model to be further applied for numerical flow and transport simulations. During this master thesis, the seismic profile line Oc270_029 was primarily re-processed in the time domain. Following the steps of pre-processing, a Kirchhoff pre-stack time migration approach was executed, resulting in an enhanced time-migrated image. On the base of this time-migrated section, horizon interpretation was performed to proceed with the depth imaging of the seismic data.

As a first step, an interval velocity model was derived as a function of depth by standard semblance analysis of the seismic data. This velocity model was used in a Kirchhoff pre-stack depth migration, resulting in a first subsurface model. Subsequently, the velocity model was refined by horizon- and grid based tomography approaches and an updated Kirchhoff pre-stack depth migration result was calculated using this new velocity models. Interpretation of previously identified sequences by Miller et al. (2013a) on the depth-migrated stack of Oc270_029 is concluding this thesis.

Acknowledgement

I would first like to thank my thesis advisor Dr. Sönke Reiche of the Faculty of Applied Geophysics and Geothermal Energy (E.ON Energy Research Center) at the RWTH Aachen University. He supported me greatly and was always willing to help me.

In addition, I would like to thank my supervisors at TU Bergakademie Freiberg, Dr. Marko Riedel and Prof. Stefan Buske, for their valuable guidance and the wonderful collaboration. You definitely provided me with the tools that I needed to choose the right direction and successfully complete my thesis. I would like to especially express my very sincere gratitude to Dr. Marko Riedel, who offered his continuous advice and encouragement throughout the course of this thesis. It was a great pleasure to work as part of this joint research project within your research group and I had a wonderful time during my stay in Freiberg.

I would also like to thank all scientist of cruise Oc270 and IODP expedition Leg 313 for providing the seismic data as well as the other data sets which made this thesis possible.

Thank you to my parents and my sister who always supported me during the years of my studies and to Michiel Ooms who was always on my side, even when he had to finish his thesis simultaneously. I could not have done it without you.

Thank you very much everyone!

Kira Aßhoff

Etteln, 10.08.2016

Contents

List of Abbreviations

NJ	New Jersey
2D	two dimensional
3D	three dimesional
ODP	Ocean Drilling Program
IODP	International Ocean Discovery Program
LST	lowstand system tract
HST	highstand sytem tract
TST	trangressive system tract
TS	Transgressive surface
MFS	Maximum flooding surface
TWT	Two-way travel time
1D	one dimesional
P-wave	primary wave
S-wave	shear wave
4D	four dimesional
CMP	Common mid point
CDP	Common depth point

DMO Dip moveout

NMO Normal moveout

TAR True Amplitude Recovery

rms root-mean-square

MVA Migration velocity analysis

CIG Common image gather

ODCIG Offset-domain common image gather

CRP Common reflection point

RMO Residual Moveout

UTM Universal Transverse Mercator

AGC Automatic gain control

SRME Surface-related multiple elimination

CHAPTER 1

Introduction

In the first chapter, the subject of this thesis will be introduced. Next, the main research question and methodology are presented. This chapter is concluded with the outline of this thesis.

1.1 Motivation and Objectives

In 2009 the New Jersey (NJ) shelf was most recently targeted by the scientific drilling campaign IODP Leg 313. Three boreholes (M27, M28 and M29) were drilled during this expedition down to 631-755 m depth at the NJ middle shelf as shown in Figure 1.5. This drilling campaign and in more detail the boreholes M27-M29 were crossed by the earlier acquired seismic profile line Oc270_529 of the R/V Oceanus cruise Oc270. In addition to the more than 5800 m of downhole logging data, groundwater samples were also retrieved along each of the boreholes at various depths with a vertical sampling rate of 9 m (Mountain et al., 2010; Lofi et al., 2013). These samples were analyzed for several characteristics like pH value and concentration of major and minor ions, which made it possible to differentiate between pore-water salinities.
The occurrence of low salinity groundwater lenses at continental margins is a global phenomenon and the NJ shelf represents one of the best documented examples (Post et al., 2013). This multi-layered system of the NJ margin is developed in the unconsolidated siliclastic deposits of Miocene times. Fresh water reservoirs with salinity lower than 3 g/L were discovered down to a depth of 400 m depth below the seafloor and their presence was documented up to 130 km far-off the NJ coast (Lofi et al., 2013). The fresh-water reservoir was originally considered to have a gradual salinity gradient at its base and a steep salinity gradient at its top, but the analyses of the water samples from IODP Leg 313 showed vertical alternations of salt-, fresh- and/or brackish-water (Lofi et al., 2013). Evidence of very complex salinity variations with depth was assured by sharp boundaries observed between salt- and fresh-water (Mountain et al., 2010).
Reasons for the freshwater distribution so far-off the coast are still unknown but it is found that the processes which may control the salinity are mainly influenced by lithology, porosity, and permeability. Two conflicting hypotheses about the occurrence and the recharge system of the more complex fresh water distribution at the NJ shelf are still in an ongoing debate since evidence for their certainty was established for both (Hathaway et al., 1979; Lofi et al., 2013):

1. During the Pleistocene glacial period, large parts of the NJ shelf were subaerially exposed and fresh groundwater was emplaced due to rainwater infiltration and enhanced offshore directed fresh groundwater discharge (Cohen et al., 2010).

2. Onshore aquifers are directly dynamically connected with the offshore fresh groundwater bodies which are constantly recharged by seaward-flowing meteoric groundwater.

Studies from Lofi et al. (2013), McAuley et al. (2001), Cohen et al. (2010) and Post et al. (2013) give indications for the first hypothesis. As described by Figure 1.1a, during glacial periods the sea level fall is followed by subaerial exposure of the shelf and is then influenced by precipitation and an increased hydraulic head results in an improved offshore fresh groundwater flow. This effect is reversed during the interglacial period with the rising sea level (Figure 1.1b). As a result of the rising sea level, the shelf is flooded, seawater is intruding and accordingly the hydraulic head is decreasing. Submarine fresh groundwater discharge is reduced (Post et al., 2013). Research by Lofi et al. (2013) shows that the fresh water is preferentially stored in fine-grained and low-permeability deposits at the NJ shelf, whereas salty water occupies coarse-grained and high-permeable units. Furthermore, it has been found that the transition from fresh-water to salt-water boundaries is often marked by permeability barriers which control the salinity distribution (Lofi et al., 2013). These observations support the hypothesis of the Pleistocene fresh groundwater emplacement.
Chemical analysis of the water samples from the IODP Leg 313 drilling locations evaluated by van Geldern et al. (2013) reveal a similarity between the chemical composition and by this especially the stable isotope ratios of the samples and values of present precipitation of the NJ shelf. The discovery of this similarity supports the second hypothesis because it indicates that the fresh-water may be there due to an ongoing recharge by offshore groundwater flow, or it was accumulated during a period with similar hydrological and climatic conditions as at present now (van Geldern et al., 2013). On the contrary, the permeabilty model composed by Lofi et al. (2013) does not support the assumption of a dynamic connection between the onshore aquifers and the recharge system. Furthermore, Kooi and Groen (2001) simulated the groundwater flow under the condition of a present-day hydraulic head, and the results indicate an insufficiency of the hydraulic head, making a dynamically ongoing recharge by offshore groundwater impossible.

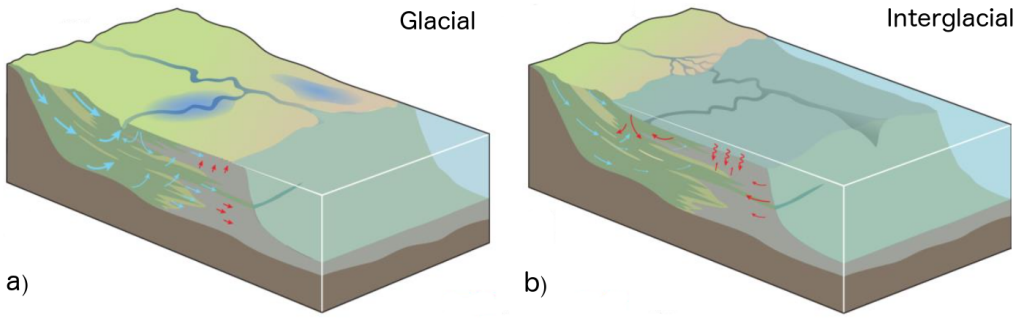

Figure 1.1: During glacial periods (a), a low sea level stimulates offshore fresh groundwater discharge and more offshore fresh groundwater flow, whereas during interglacial periods (b) the shelf is flooded, seawater is intruding and offshore fresh water discharge is reduced. The red arrows highlight intruded seawater while the freshwater flow is indicated by light blue arrows (adapted and modified after Post et al. (2013)).

A better understanding of these vertical salinity variations and the controlling factors of groundwater circulation at the NJ shelf is the aim of the joint research project of the TU Bergakademie Freiberg and RWTH Aachen University. Several geological, geophysical and petrophysical studies were previously performed in this area during earlier expeditions, including multiple 2D and 3D seismic surveys. A reliable 3D subsurface model can be derived from these seismic data sets, and combined with core and logging data from several ODP and IODP expeditions leading towards numerical simulations of the fresh water emplacement and recharge system at the New Jersey shelf. Moreover, to attain the purpose of simulating the submarine groundwater flow at the NJ shelf in a realistic way, a 3D hydrogeological model has to be built. Only a numerical model constrained by seismic, core and logging data can potentially resolve the complex distribution of vertical salinity changes and provide information concerning the two conflicting hypotheses.
In order to perform these numerical simulations, the 3D structural subsurface model has to be built, resembling the geometry of the depositional layers and their inherent physical properties in a most realistic way. For this purpose, depth-migrated seismic data is needed since it can image the subsurface realistically. As part of this thesis the seismic line Oc270_029 from the seismic data set acquired during cruise R/V Oc270 will be processed and imaged in depth. Since several seismic lines are required for building a reliable 3D subsurface model of the NJ shelf, a processing workflow has been constructed at TU Bergakademie Freiberg. Based on this processing workflow, a depth-migrated image of the subsurface will be provided. Line Oc270_029 was already processed earlier by Miller and Mountain (1994), with a time-migrated section as their final result. The main objectives of the current work are to re-process the seismic line to achieve an enhanced time-migrated image and to conclude with a newly constructed depth-migrated section. Additional objectives are: improving the signal-to-noise ratio, enhancing the reflector continuity, suppressing multiples and a refined velocity model. A satisfyingly processed depth-migrated section can contribute to constructing the most realistic 3D subsurface model of the NJ shelf. Time migration, as well as conversion in depth, will be performed with the help of a 2D Kirchhoff pre-stack migration approach.

1.2 Study area and geological setting

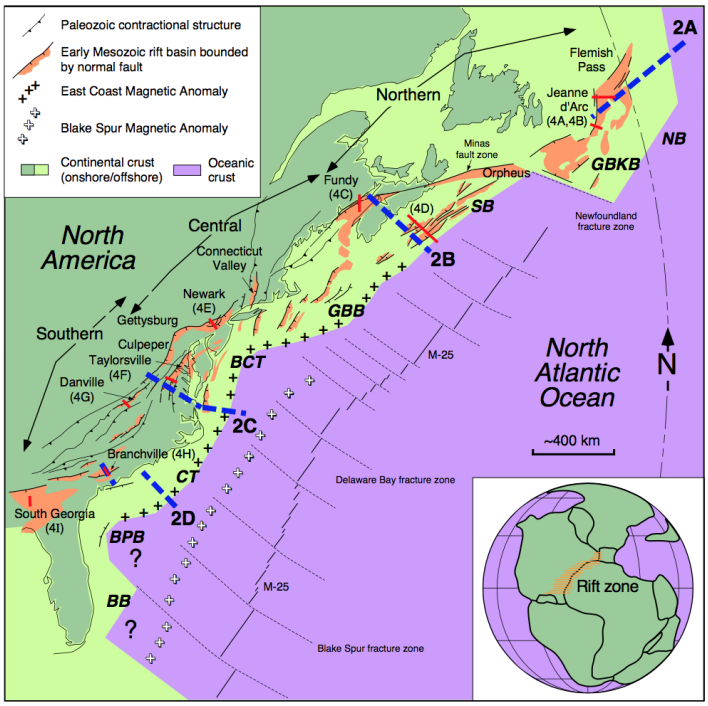

Figure 1.2: Contractional structures of the Paleozoic and early Mesozoic rift basins of eastern North America. Important tectonic features and anomalies of the North Atlantic Ocean are indicated (adapted from Withjack and Schlische (2005)).

The NJ margin is located offshore the east cost of North America as part of the US Atlantic region.

The formation process of the NJ margin starts in the early Mesozoic time when a massive rift zone developed within the Pangean supercontinent, which split up millions of years later and left behind extinct fragments of this rift zone due to seafloor spreading in the Early to Early-Middle Jurassic (Withjack and Schlische, 2005; Withjack et al., 2012). One of these fragments is the North American margin. Withjack et al. (2012) divided the North American margin into three geographic segments with the NJ shelf, slope and rise building up the central segment of the North American rift system (Figure 1.2).

Subsequent tectonism in the NJ margin was mainly controlled by passive effects like thermal subsidence, sediment loading and thermoflexural subsidence (Kominz et al., 2002; Miller et al., 2013a). It can be classified as a classic passive margin which is dominated by siliclastic sedimentation (Miller et al., 2014). Apart from minor local normal faulting, a single Early Cretaceous igneous intrusion and rare salt diaprism, the history of the NJ passive margin post-rift tectonism is rather simple (Poag, 1985). While most of the glacial isostatic adjustments are observed as far-field effects, some near-field glacial isostatic adjustment effects had an influence on the shelf-slope sedimentation when during the major Pleistocene glacials the continental ice sheets extended to northern NJ (Miller et al., 2014).

It is well known that the NJ margin is a good natural laboratory and a great indicator for research on a variety of different topics like the evaluation of depositional sequences and sea-level changes as much as the change of the sedimentary flux. Further characteristics of this margin are good tectonic stability, strong architecture and sediment compositions distinguished by thick Miocene sediments (Miller et al., 2013a; Lofi et al., 2013). The NJ shelf is an optimal

study area for the sedimentary response to sea-level changes. Sea-level changes are closely tied to the sequence stratigraphy which is based on the appearance of sedimentary units on logs, coring data and seismic profiles. In principle, the recognized sequences are subdivided into lowstand system tracts (LST), transgressive system tracts (TST), falling stage system tracts or highstand system tracts (HST) and further defined by the two stratal surfaces which are called the transgressive surface (TS) and the maximum flooding surface (MFS) (Figure 1.3). These system tracts are deposited during a specific phase of the relative-sea level cycle (Miller et al., 2013b).

Early studies of the sequence stratigraphy of the NJ shelf are primarily based on several multi-channel seismic data sets (Exxon, Ew9009, Oc270, CH0698). Starting with the industry seismic profiles by Exxon, Greenlee (1988) and Greenlee et al. (1988) recognized the NJ shelf as a typical example of Miocene prograding sequences. Prograding sequences which are bound by sigmoidal or so-called S-shaped surfaces are referred to as clinothems. Such a sequence stratigraphical setting is described by the clinothem model in Figure 1.3. Based on the seismic results of cruise Ew9009, the presence of thick lowstand wedges, HST and a seismic lack of TST were interpreted within Miocene sequences beneath the middle to outer NJ continental shelf (Greenlee et al., 1992; Miller et al., 2013b). The interpretation of the seismic data from the outer continental shelf (Oc270) confirms the occurrence of only LST and HST. The most recent seismic grid from cruise CH0698 is mainly focussed on the landward part of the NJ shelf. Monteverde et al. (2008) came to similar conclusions about the thicknesses of the LST and HST by interpreting these profiles. The fact that TST is either absent or below seismic resolution appears to conform the previous research.

IODP Expedition 313 disclosed new information regarding the sequence stratigraphy of the drilling site. Due to sediment recovery in the boreholes M27, M28 and M29 of the IODP Expedition Leg 313, Mountain et al. (2010) subdivided the sediments into eight lithostratigraphic units of Late Eocene to Late Pleistocene age. Identification of the sequence boundaries and stratal surfaces was done by integrating the reflector termination of seismic profile line Oc270_529, physical stratigraphy in boreholes (lithofacies succession, gamma logs, benthic foraminiferal paleodepth trends) and age breaks indicated by Sr isotope stratigraphy or biostratigraphy (Miller et al., 2013b). Results of the seismic-core correlation are confirmed by synthetic seismograms and predict the depth of the seismic sequence boundaries which made it also possible to connect the recognized unconformities to the core and logging data. They

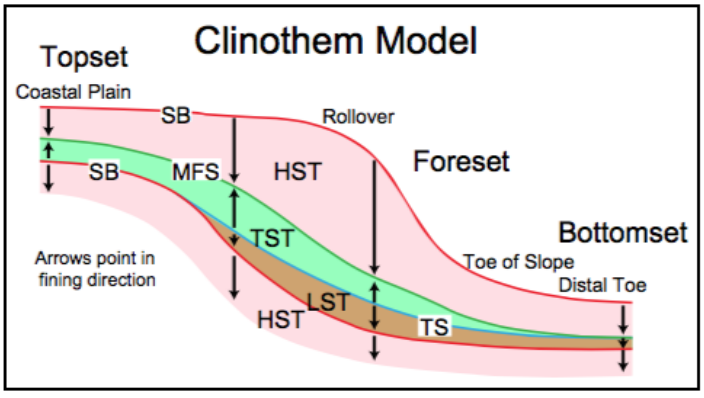

Figure 1.3: Clinothem model adapted from Miller et al. (2013b). Fining direction is equivalent to deeping direction.

also show the influence of unconformities as a source for impedance contrast and thus seismic reflections (Miller et al., 2013a). Overall it was possible to identify more than 20 seismic sequences within the seismic profile. Several depositional cycles were especially identified within Oligocene-Miocene sequences and related to relative changes in sea level (Miller et al., 2013b). Figure 1.4 shows the upper seven lithostratigraphic sequences and small scale interval sequence boundaries along the seismic profile crossing the IODP Leg 313 drilling project. In contrast to earlier studies, drilling through the foreset location of the NJ shallow continental shelf reveals thick HST, thin TST and thin LST. Thus, the absence of TST is refuted for this profile. In addition to this, more details like regressive patterns in HST and LST are shown in the cores (Miller et al., 2013b). As discussed in detail by Mountain et al. (2010) and Lofi et al. (2013), the main sedimentary facies range from clay to sands in places where the topset facies is composed of well-sorted silts and sands, whereas the bottomset facies consists of silts and silty clays.

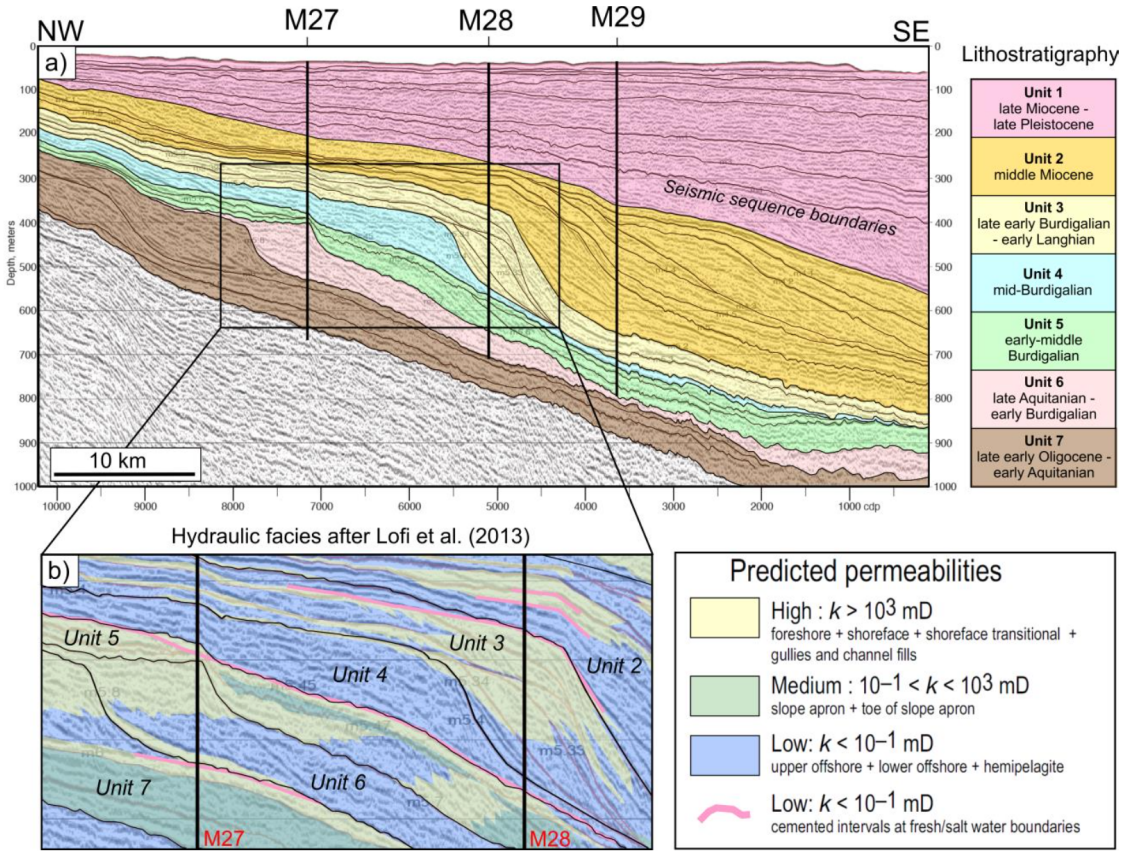

Figure 1.4: Seismic line OC270_529 across the drilling locations M27, M28 and M29 of the IODP expedition Leg 313. Seven major lithostratigraphic units subdivide the sedimentary series. Additional subdivisions of the major units into additional small-scale seismic sequence boundaries are represented by black lines (adapted and modified after Lofi et al. (2013) and Mountain et al. (2010)).

1.3 Previous studies in seismics

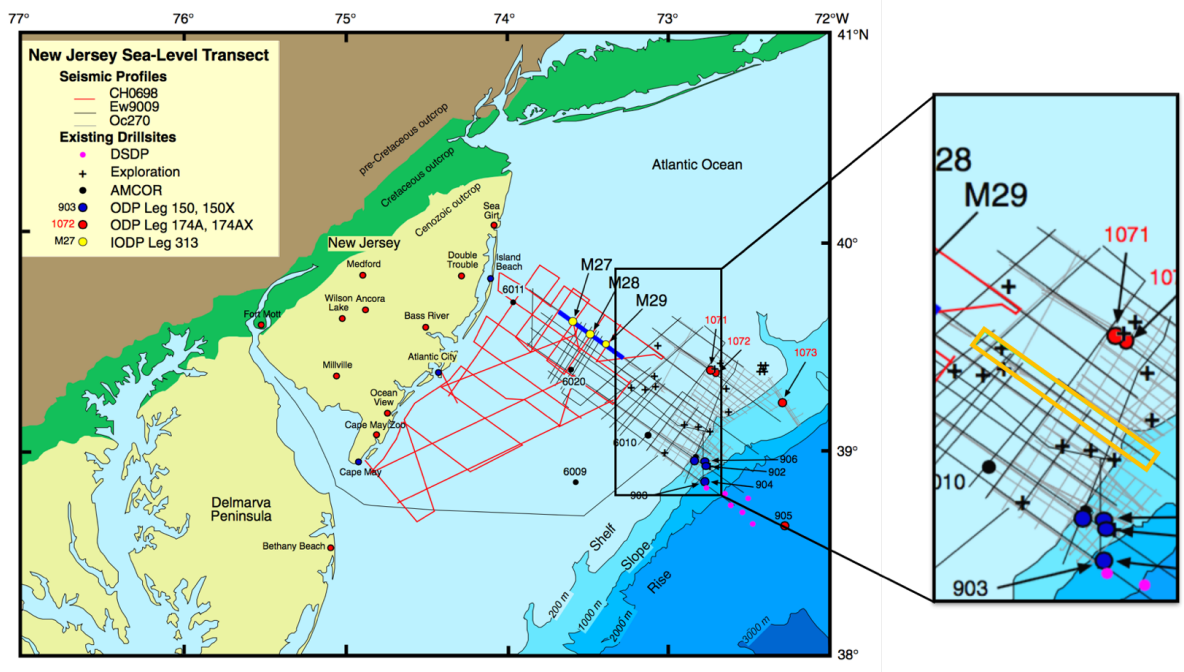

Figure 1.5: Three sets of multichannel seismic acquisitions (R/V Ewing cruise Ew9009, R/V Oceanus cruise Oc270, and R/V Cape Hatteras cruise CH0698) are shown as well as IODP Expedition 313 sites (M27, M28 and M29) together with previously completed onshore core-holes, and offshore core-holes drilled by the Atlantic Margin Coring Program (AMCOR), the Ocean Drilling Program (ODP), and Integrated Ocean Drilling Program (IODP) (Hathaway et al., 1979). Seismic profiles are shown by black, red and gray lines. To the right, an enlarged section is shown where the orange box shows the area of the processed seismic line Oc270_029 (adapted and modified after Miller et al. (2013a)).

Acquisition of seismic profiles along the NJ shelf has been an important aspect of gaining more knowledge about the geological and structural setting of the margin. Several seismic grids, which were acquired from 1990 to 1998, build an extensive set of seismic data across the NJ shelf. Figure 1.5 gives an overview of the three most important seismic data sets available for building a realistic 3D subsurface model in the area of interest.

1. Poor resolution of the multichannel seismic data set acquired by Exxon (1975-1977) and the fact that prograding clinothem sequences were unresolved for this data, made it necessary to shoot a new exploration grid. During the cruise Ew9009 on the R/V Ewing in 1990, a new seismic grid was shot across the shelf and slope (Figure 1.5, black lines). The main objective of this project was to determine the geometry of the Oligocene to Miocene depositional sequences which could not be resolved by the older seismic data and to use the recorded data as a base for the planned continental shelf-to-slope drilling program ODP Leg 150. This program should further define the Oligocene to Miocene depositional sequences and relate their geometry to changes in relative sea-level. To achieve a good vertical resolution of around 15 m, a 120 channel and 6 air gun system was used (Table 1.1) (Miller et al., 2013a; Lofi et al., 2013; Monteverde et al., 2008).

2. In 1995 a seismic data set of a higher resolution was shot by the R/V Oceanus cruise Oc270 (Figure 1.5, gray lines). While this cruise primarily collected seismic data at the outer

NJ margin, it has also improved the resolution of features imaged during Ew9009. Furthermore, line 529 has been used as the base for the drilling campaign during the IODP Leg 313 for the sites M27-M29. A 48-channel streamer and a GI-gun as a source were used to achieve a vertical resolution of 5 m with sufficient clarity down to 1.3 s of two-way travel time (TWT) (Table 1.1) (Miller et al., 2013a; Lofi et al., 2013; Monteverde et al., 2000, 2008; Austin et al., 1996).

3. Figure 1.5 (red lines) shows, that the seismic data acquisition during survey CH0698 was concentrated on the inner coastal region of the continental margin. It links the middle shelf to onshore NJ and was recorded in 1998, which makes it the latest acquired seismic data set shown in Figure 1.5. The same equipment was deployed as during Oc270 (Table 1.1) and the three acquisition grids vary between 150 to 600 m line spacing adding up to an overall collected seismic grid of around 1100 km. The main objective was to provide more detailed information on clinothem geometries as well as building the base for the Expedition 313 and the locations for the boreholes M27, M28 and M29, similar to the Oc270 cruise (Miller et al., 2013a; Monteverde et al., 2000, 2008).

The most recent results focused on the interpretation of Oc270 line 529 which crosses the IODP 313 drill sites and could thus jointly be interpreted with the collected core and logging data. After successfully fulfilling the drilling campaign IODP Leg 313, the seismic data of profile Oc270_529 was further used for seismic-core correlation. For this task, a 1-D velocity function by Mountain and Monteverde (2012) converted the time-migrated section into depth. A 1-D velocity function does not reflect the subsurface realistically, but since the core information is available, the depth at these locations can be correctly estimated. A workflow, constructed by the TU Bergakademie Freiberg, leads to an updated image of this profile, considering a detailed velocity model and enhanced processing steps towards a depth-migrated section (Riedel et al., 2016b).

Table 1.1: Data acquisition parameters for the cruises Ew9009, Oc270 and CH0698.

Cruise	**Year**	**Source**	**Receiver**	**Resolution**
Ew9009	1990	mainly Airgun-array (1350 in^3)	mainly 1500 m-long, 120-channel streamer	15 m vertical
Oc270	1995	GI-Gun (105/45 in^3)	600 m-long, 48-channel streamer	5 m vertical
CH0698	1998	GI-Gun (45/45 in^3)	600 m-long, 48-channel streamer	5 m vertical

1.4 Outline

This Master's thesis on the re-processing and depth imaging of the 2D marine seismic data from the area of the NJ shelf is structured as followed:

- Chapter 2 is a short introduction to the theory of seismic processing, Kirchhoff pre-stack migration and tomography.
- Chapter 3 gives an overview of the steps of pre-processing of the seismic data.
- Chapter 4 discusses the results achieved during processing and identified reflectors are interpreted.
- Chapter 5 concludes the thesis and offers an outlook.

CHAPTER 2

Theory

2.1 Seismic wave propagation

This section gives a short introduction on the topic of seismic wave propagation, following the explanations in the second edition of 'Fundamentals of Geophysics' by Lowrie (2007) and the book 'Seismic Data Analysis: Processing, Inversion, and Interpretation of Seismic Data' by Yilmaz (2001). It will be complemented by the principal aspects of a seismic survey and seismic processing.

Seismic wave propagation through a heterogeneous medium is an extremely complex process. The fundamental properties of matter underlie wave propagation, the restoring character largely depending on the state of the medium (Wapenaar and Berkhout, 1989). Starting at a point source, seismic disturbances are propagating through the medium without destroying the medium. After releasing seismic energy from the point source, the energy is transmitted as a complex set of wave motions and the particles of the affected medium carry out simple harmonic motions. The released energy splits up into so-called seismic body waves which propagate through the medium and into a remaining part which spreads out the energy over the surface of the medium, as a seismic surface wave. Seismic body waves also called elastic waves, can be further separated into P- and S-waves. The compressional wave (P-wave)propagates longitudinally through the medium and propagates through it as a set of compressions and dilatations. The particle motion is an oscillation parallel to the direction of propagation. Of all seismic waves the compressional wave is the fastest out and consequently, it is called primary wave or P-wave. The velocity of the P-wave is described by the bulk modulus, given by K[Pa] $= \lambda + \frac{2}{3}\mu$, with the shear rigidity modulus μ $[\frac{N}{m}]$ and the Lamé constant λ $[\frac{N}{m^2}]$. Therefore, the P-wave velocity and the elastic properties are related by:

$$v_p = \sqrt{\frac{\lambda + 2\mu}{\rho}} = \sqrt{\frac{K + \frac{4}{3}\mu}{\rho}} \quad , \tag{2.1}$$

with ρ $[\frac{kg}{m^3}]$ being the density. From Equation 2.1 and the compressibility being nonzero (K $\neq$ 0), it follows that P-waves can travel through solids, liquids and gases.

The name S-wave or secondary wave is based on the fact that these shear waves travel more slowly through the medium than P-waves. It is characteristic of S-waves that the particle motion is an oscillation perpendicular to the direction of propagation. Another characteristic is described by Equation 2.2. The velocity of the shear waves is only determined by the elastic

property of the rigidity μ and since μ is zero in liquids and gases, shear waves can not propagate in these media. The shear wave velocity is given by

$$v_s = \sqrt{\frac{\mu}{\rho}} \quad . \tag{2.2}$$

The motion of the waves is characterized by several aspects as it is known that a seismic wave is an oscillation and the amplitude variations can be represented by *sine* and *cosine* functions, while the time it takes between two successive peak amplitudes is given by T [s]. It follows a repeatable pattern in time as well as in space and transmits energy by means of elastic displacement. Frequency (f [Hz]) which equals the inverse of the period, is a measure of how often the amplitude is repeated per second. Furthermore, the wavelength λ is the quotient of the velocity and frequency. As a consequence, the speed of a seismic wave can also be expressed as:

$$v = \lambda * f \quad . \tag{2.3}$$

Changes in the properties of the medium lead directly to a change in the behavior of the seismic wave. Huygens' principle of a first wavefront causing a secondary wavelet after the particles of the original wavefront are agitated, can be used to derive the principles of reflection, refraction, and diffraction of seismic waves at an interface. The determination of the medium, in which acoustic motion takes place, is based on the variations of elastic parameters between rock types. A change in acoustic impedance of a medium will lead to reflection or refraction of the seismic wave at that interface. The acoustic impedance is defined as the product of velocity v_p and density ρ, and a change in one of these two values generates the adjustments in the ray path of the elastic waves. The way a seismic wave travels from one medium to another is described by Snell's law according to which the angles measured between the ray paths of the P- and S-waves and the normal to the interface are i_p and i_s in case of reflection. Corresponding angles in the case of refraction are r_p and r_s (Figure 2.1)

$$\frac{\sin i_p}{\alpha_1} = \frac{\sin i_s}{\beta_1} = \frac{\sin r_p}{\alpha_2} = \frac{\sin r_s}{\beta_1} \quad . \tag{2.4}$$

As described by Snell's law the incoming wave travels with a velocity α_1 and encounters the interface at an angle i_p where the wave is either reflected or refracted. In the case of reflection basically, two options are possible. On the one hand, the wave may be reflected and converted from P-wave to S-wave and the wave is reflected at an angle i_s, from now on traveling at the velocity β_1. On the other hand, if the wave is not converted, it is reflected at the incident angle i_p and travels with the same velocity as before. The incoming wave can also be refracted at the interface, which means the wave continues to travel in the second layer but with a changed velocity α_2 and at a different angle r_p. Converted refracted waves are therefore traveling with β_2 and at an angle r_s. A special case is given if the wave is refracted with an angle of 90° from the normal to the boundary. This is called the critical refraction, where such waves travel parallel to the boundary in the medium with the higher velocity α_2. For rays with incident angles larger than the critical angle, refraction is no longer possible and they are almost completely reflected back into the first layer.

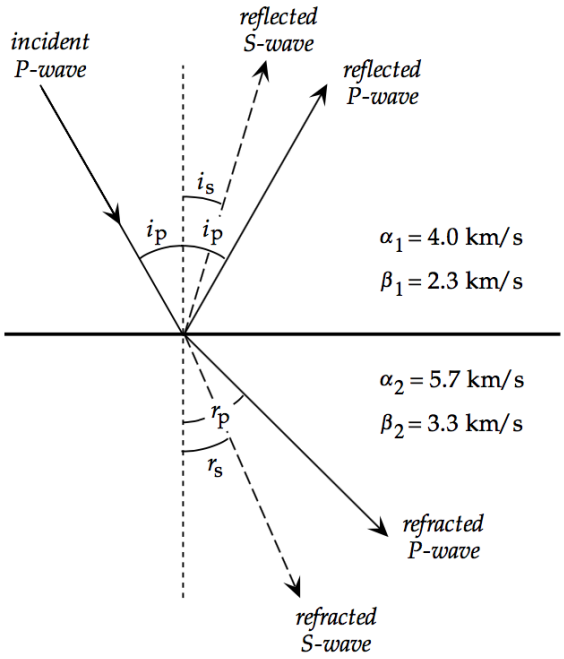

Figure 2.1: Reflected and refracted P- and S-waves are generated from a P-wave incident and a two layer interface (adapted from Lowrie (2007)).

2.2 Data Acquisition and Processing: Marine Reflection Seismology

2.2.1 Acquisition

In the case of seismic surveying, the reflection seismic method is used to evaluate the subsurface. It is a method to detect the depth of reflecting surfaces and the seismic velocities of subsurface rock layers. It follows the basic principle that a seismic impulse is used to generate the reflections from boundaries between rock layers that are characterized by differences in acoustic impedance.

A marine seismic survey is commonly acquired after a specific acquisition scheme composed of a seismic source and receivers. Figure 2.2a-c shows a classical acquisition scheme for a 2D marine reflection seismic survey. After a shot is released at the source, signals are recorded by the receivers. These waves either travel directly from the source to the geophones or are reflected at the subsurface. For triggering the seismic signal a wide choice of sources is available which can be further subdivided into chemical, mechanical, electrical and hydraulic sources. Airguns are a specific kind of a hydraulic source and are the most common ones used in marine reflection seismology. They operate according to a certain pattern that first of all compressed air is released as a rapid expansion into the water, which creates the desired signal. Since such an expansion is released again after a fixed distance with the same adjustments, the created signal is also reproducible with respect to frequency content and the wavelet signature Hübscher and Gohl (2014). For recording these signals several receivers are dragged behind the source in predetermined intervals. Hydrophones are the most commonly used sensors in marine seismic. Those receivers can be combined to a group of hydrophones which is then known as a seismic

streamer. The streamer is varying in length depending on the number of hydrophones. An optimal towing depth of the streamer has to be defined so a destructive interference with the frequencies of the source has to be prevented. After (Hübscher and Gohl, 2014), a quarter of the wavelength of the expected seismic signal is the optimal towing depth.
It is important to prevent aliasing in time and space by sampling the signal in sufficiently small time intervals and to choose a good receiver distance. Waves which are reflected several times at the boundaries are called multiples and a common reflection at the water surface is the so-called ghost. Multiples should be removed from the data during image processing. Noise from other different natural and anthropogenic sources has to be avoided.
Recorded signals are plotted as a 2D-cross-section along the profile. It is also possible to acquire a 3D survey which then covers the subsurface in a grid. In special cases like for hydrocarbon exploration, even a 4D seismic survey is an option. A 4D seismic survey is by definition a 3D survey repeated over a period of time to detect changes in the subsurface, e.g. during hydrocarbon production.

2.2.2 Processing

Processing of seismic data comprises several techniques that are used to improve the acquired data. The resolution in raw seismic data can be distorted by numerous reasons, noise being the most prominent one. The term seismic resolution commonly refers to an enhancement of the signal-to-noise ratio and the reflector continuity as well as noise suppression. During processing, multiples and noise are removed, a velocity model representing the geological layers is built and repositioning of receivers at geological structures is performed. This leads to a higher signal-to-noise ratio and a more accurate representation of the subsurface. Improved representation of the subsurface means a better understanding of the geology, which is essential for seismic interpretation.
Overall, the 2D marine seismic acquisition is based on a common midpoint (CMP) or common depth point (CDP) processing. A CMP is defined as the midpoint between source and receiver position. The geometrical arrival from shot to receiver all reflect right below the midpoint between the source and receiver for flat layers, and thus the reflection points in the subsurface then only differ in depths for that simplified case (Lowrie, 2007)(Figure 2.2d). Under regular conditions, the reflection is firstly recognized by the receiver closest to the source and the offset between the source and the following receivers causes the travel time of the reflection to be longer (Figure 2.2a-c). This effect of increasing travel times with increasing offset is termed as normal moveout (NMO) (Hübscher and Gohl, 2014). Therefore the term CDP has to be further introduced. For flat layers, the CDP is vertically below the CMP, but in the case of dipping beds, there is no CDP shared by multiple sources and receivers, so to reduce smearing of the data dip moveout correction (DMO) is necessary. DMO is the extension of the NMO correction in case dipping beds exist.
In the CMP gathers, seismic events appear as hyperbolic events. Hyperbolic events are a result of the increase in travel time of a reflected event as a consequence of increasing distance of the receiver away from the seismic source (Figure 2.21-3) (Yilmaz, 2001). In seismic processing, the image of the subsurface should be independent of this extra time delay and NMO correction is

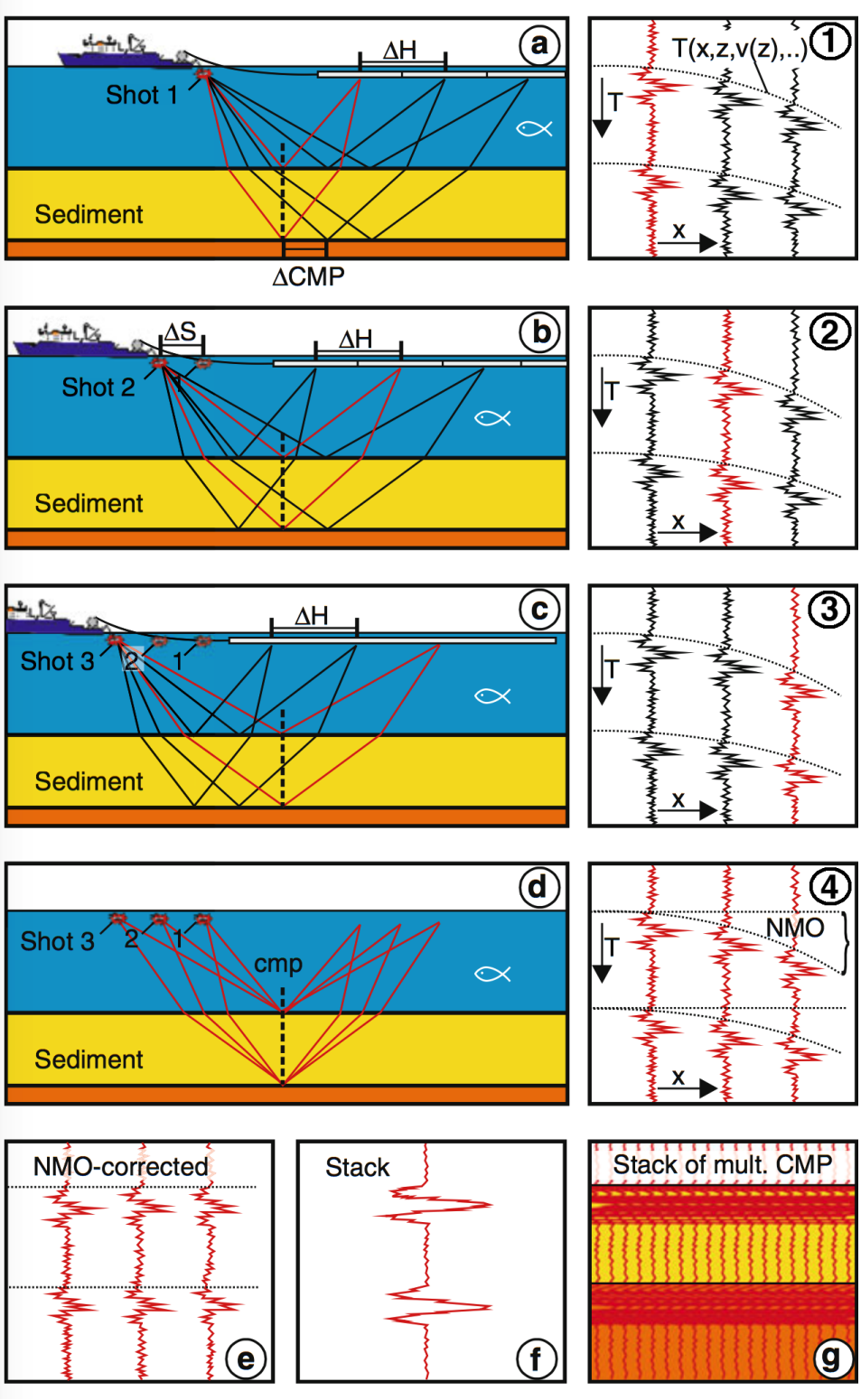

Figure 2.2: Acquisition scheme of a CMP-based 2D multichannel seismic survey. (a)-(d) describe the acquisition of the seismic data. The occurence of the effect of increasing travel times with increasing offset is given by the Subfigure (1)-(4). The process from correcting the hyperbolic moveout (NMO) towards a stacked image is shown in Subfigure (e)-(g) (adapted and modified after Hübscher and Gohl (2014))

applied according to Equation 2.5

$$t = t_0(1 + \frac{x^2}{c^2 t_0^2})^{\frac{1}{2}} \quad , \tag{2.5}$$

x being the source-receiver distance, c is the stacking velocity and t_0 is the time at zero offset. The extra time delay is described by the factor $\frac{x^2}{c^2 t_0^2}$. NMO correction is the removal of the extra time delay due to normal moveout (Yilmaz, 2001)(Figure 2.24). A result of the NMO correction should lead to the correction of a hyperbolic moveout of the traveltime curve to horizontal interfaces in the CMP gathers (Figure 2.2e). The correction is dependant on the stacking velocity model. The velocity analysis procedure involves comparing a series of stacked traces in which a velocity spectrum is applied for NMO (Taner and Koehler, 1969). Velocities are picked for reflecting events in a semblance plot. For data processing, the individual shot records are sorted into CMP gathers, NMO corrected and stacked. Stacking is defined as the summation of all NMO corrected CMP gathers to one single trace as shown in Figure 2.2f. Subsequently, the stacked CMP traces are displayed along the seismic profile, which results in an image of the subsurface (Hübscher and Gohl, 2014)(Figure 2.2g). Stacked data has the main purpose to improve the signal-to-noise ratio caused by adding up reflections constructively while noise cancels out. The data processing is a very extensive methodology which can always be further refined. In this thesis, only the most fundamental processing steps are exemplified. The final step in seismic data processing is the seismic migration in the time or in the depth domain (Yilmaz, 2001).

Frequency Filter

Frequency filter removes data within a predefined frequency range and may thereby suppress the unwanted events. Coherent, random and ambient noise, like swell noise and noise generated from the outside (ship, waves, etc.), are the main factors which have to be filtered out. By using frequency filtering, the coherent, as well as the incoherent noise, can be suppressed in the data. For frequency filtering commonly a single zero-phase Ormsby bandpass filter is applied to the seismic data. A zero-phase filter is composed of the frequencies wich are building the wavelet that is used during the filtering process. The Ormsby bandpass filter is defined as a trapezoidal-shaped filter and is specified by four corner frequencies [f1, f2, f3, f4] which band limit the amplitude spectrum of the seismic traces. The filter removes frequencies higher than corner frequency f4 and lower than corner frequency f1. To ramp up the removal of the frequencies, corner frequencies f2, and f3 are in included. The filter has a ramped shape to avoid ringing, the so-called Gibbs phenomenon, and a slightly gentler slope on the high-frequency side (Yilmaz, 2001). This kind of bandpass filter is preferred since acquired seismic data contains low-frequency noise as well as high-frequency noise. Frequency filtering can be performed during different stages in data processing, such as before deconvolution or before velocity picking (Yilmaz, 2001).

True Amplitude Recovery

One of the first tasks which improve the data quality is the True Amplitude Recovery (TAR). In an ideal way, it should be possible to relate directly from the reflection amplitudes to the change in rock properties. The amplitude of the seismic data has to be adjusted in a way by the amplitude recovery that it compensates for effects like spherical divergence and attenuation. Equation 2.6 is used for calculating TAR:

$$A(t) = A_0(t) \cdot k \cdot t^n \quad , \tag{2.6}$$

$A(t)$ is the output amplitude, $A_0(t)$ is the initial amplitude, t is the travel time, k is the cut-off time and n is an exponential factor (Yilmaz, 2001).

Deconvolution

Several deconvolution techniques are available like spiking deconvolution, Kalman filtering, deterministic deconvolution and predictive deconvolution. The technique of predictive deconvolution will be explained in detail.
This procedure of predictive deconvolution includes a prediction process, for which prediction filters are used. In principle, values for a time-advanced predictable signal $(t + \alpha)$ of the input series $x(t)$ should be estimated. After Wiener (Robinson and Treitel, 1980) is it possible to receive the desired signal, $x(t + \alpha)$, by taking the autocorrelation of input traces for the filter design. α is defined as the prediction lag. Commonly, seismic data has a predictable component which are the multiples and an unpredictable component referred to as the reflections. The goal of predictive deconvolution is to first of all estimate the predictable information of the seismic traces and afterward remove these parts. By removing the predictable part only the unpredictable part (reflections) is preserved by evaluating the autocorrelation. Samples of the autocorrelation ranging from *0* to α express the part of the wavelet which are kept and control the resolution, while samples from $\alpha + 1$ to $n + \alpha$ gives the suppressed part, with n as the operator length. It results in an extinction of multiples since its energy is attenuated and the reverberations are removed. Predictive deconvolution can also be used to increase the temporal resolution due to wavelet compression and by altering the amplitude spectrum. Ideally, only the earth real reflectivity in the seismic trace should be remaining.
To ensure numerical stability prewhitening is introduced before deconvolution. Prewithening is defined as an artificial level of white noise *(ε)* which is obtained by adding a constant to the autocorrelation function. Therefore, deconvolution is computed by the operator length n, prediction lag α and white noise level ε (Yilmaz, 2001).

Radon Filter

The Radon transform is a mathematical technique, used in seismic data processing and image analysis. Several types of Radon transforms are known and implemented for multiple-attenuation techniques in seismic data processing. The three most common transform techniques are the slant-stack or $\tau - P$ transform, the hyperbolic Radon transform and the parabolic Radon transform (Trad, 2001). A special case of the Radon transform is the parabolic $\tau - P$ transform, which was adopted for this thesis. For this transform, the data is summed along a parabolic path in the time-offset domain expressed as followed:

$$S(\tau, P) = \sum d(t = \tau + Px, x) \ . \tag{2.7}$$

In this case τ, which is the two-way intercept time, and P also known as slowness, slope or parabolic tracks, represent the two axes of the space. P is defined by the velocity and the incidence angle θ ($P = sin\theta/v$). $S(\tau, P)$ is the plane wave and $d(t, x)$ represents a shot where t is the two-way travel time and x is the offset (Trad, 2001). Primary reflections can be distinguished from multiples based on the residual moveout from near to far offset. In practice, the Radon $\tau - P$ transform requires the application of a top or bottom mute in the Radon domain which cuts off the unrealistic velocity information, a multiple produces. This technique implies the modeling of the multiples and subtracting these multiples from the input gathers to receive the multiple-free gather. Several studies show that the Radon transformation is more effective for long-period multiples than short-period multiples (Toft and Sørensen, 1996).

2.2.3 2D - Kirchhoff Pre-stack Depth Migration

In this section the general principle of seismic migration and especially the Kirchhoff Pre-stack Depth Migration followed by reflection tomography is described on the basis of the book 'Seismic Data Analysis: Processing, Inversion, and Interpretation of Seismic Data' by Yilmaz (2001) and the book 'Concepts and Application in 3D Seismic Imaging' by Biondi (2009).
Although timing effects can be removed during the NMO correction process, remaining wave propagation effects still have to be removed to create a true image of the subsurface. Migration of seismic data is a process by which all of the reflections are relocated back to their true subsurface position and the spatial resolution is improved. Theoretically, the migration is based on the wave propagation theory and a variation of migration approaches are further subdivided due to their way of solving the wave equation. The Kirchhoff migration approach is one of the most popular ones due to its computational efficiency and flexibility. It can be physically described by the integral solution of the 2-D scalar wave equation (Equation 2.12). Depending on the complexity of the lithology and the particular kind of application, migration can be performed either in the time domain or in the depth domain. For this thesis, Kirchhoff pre-stack migration approaches in time, as well as in depth are used since pre-stack migration clearly produces a superior seismic image compared to the post-stack migration procedure.
Application of migration in the time domain will result in a time-migrated section showing the reflectors located in terms of the two-way travel time. Mild to moderate velocity variations are a prerequisite for time migration. If information about the absolute depth of the reflectors are needed, or lateral velocity gradients are significantly strong, a time migration is not sufficient any longer and only a depth-migrated section can produce the true subsurface image. Due to this, a good velocity model is of significant importance since the displacement is associated with velocity and travel time.
To get a comprehensive understanding of the background of the Kirchhoff migration, Huygens' principle has to be recalled. As mentioned in Section 2.2, a plane incident wave responds to Huygens' secondary source by generating a new semi-circular wavefront in the x-z section (Figure 2.3a). If a propagating wavefront meets a small reflection point, also referred to as a diffractor, it acts as a secondary source whose response is a diffraction hyperbola if transferred to the x-t plane (Figure 2.3b).

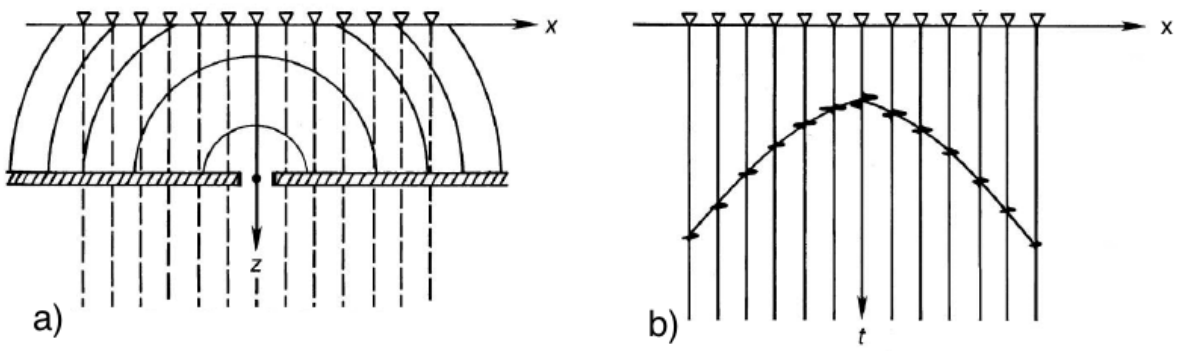

Figure 2.3: Principle of a diffractor (a) in the x-z plane and the corresponding hyperbola in the x-t plane (b) (adapted and modified after Yilmaz (2001))

A consistent reflector can be seen as a composition of many of these diffractors (Huygens' secondary sources) and many hyperbolic traveltime curves are produced, which also superpose each other. Under the condition that every point in the x-z plane acts as diffractor, the data can be added along a traveltime hyperbola which is also called a diffraction summation or a summation surface. For this, at each point along the path the corresponding seismic energy is examined and these amplitudes are summed up along the related diffraction curves.
Kirchhoff migration can basically be seen as a diffraction summation and a general expression can be written as (Schneider, 1978):

$$I(\xi) \approx \sum_{i \in \Omega_\xi} W(\xi, m, h) D[t = t_D(\xi, m, h), m, h] \ . \tag{2.8}$$

$I(\xi)$ is given as the image which is defined in the 2D space (ξ=z_ξ, x_ξ). The data D is evaluated depending on the total time delay t_D which defines the summation surfaces, and the data is weighted by an appropriate factor W. The shape of this summation surface is strongly linked to the chosen velocity function.
In the case of migration in time domain it is assumed that the velocities are locally lateral uniform and to compute a velocity model in the time domain, root-mean-square (rms) velocities are used. These are average velocities which are measured from the data by using a particular velocity spectrum which is computed from the CDP gathers after NMO correction has been applied and the flatness of the corrected gathers is estimated. Time delays (t_D) can be analytically calculated for the constant velocity of time migration by the following expression:

$$t_D^2 = t_s^2 + \frac{x^2}{v_{rms}^2} \ . \tag{2.9}$$

t_D is computed by the rms velocity (v_{rms}), distance x and t_s which results in the hyperbola at time zero.
To proceed with the conversion to the depth domain and apply the depth migration, an initial interval velocity model is needed. The rms velocity is a function of the two-way travel time and it is not possible to use these velocities to directly transform the TWT into depth. A interval velocity can be defined as the average velocity between two reflections (horizons) in the subsurface. For flat- layerd media a relation of the Dix formula makes it possible to extract interval velocities from rms velocities by the simple relationship to receive a initial interval velocty function:

$$V_{n-layer} = \Big(\frac{V_n^2 t_n - V_{n-1}^2 t_{n-1}}{t_n - t_{n-1}} \Big)^{\frac{1}{2}} \ , \tag{2.10}$$

$V_{n-layer}$ is the extracted interval velocity from the stacking velocities V_{n-1} and V_n with the reflection arrival times t_{n-1} and t_n. By using this relation, interval velocity in the n^{th} layer

can be calculated by extracting the effects vertically to the rms velocity of the overlying layer (Jones, 2010). More description concering the Eikonal equation and Dix formula is described in Yilmaz (2001).
Since the velocity is not constant any longer, the geometry of the summation surfaces becomes more complex too, and the time delay functions have to be computed numerically by solving the Eikonal equation. Ray tracing has to be performed through the interval velocity model to compute the time delays used for pre-stack depth migration.These are evaluated by adding the time delay from the source location t_s to the image point (ξ) to the time delay from the receiver location t_r to the same image point (ξ):

$$t_D = t_s[\xi, s, v(z,x)] + t_r[\xi, r, v(z,x)] \ . \tag{2.11}$$

In this case of depth migration several other corrections have to be considered like the obliquity factor and the spherical spreading factor. The first one accounts for the angle dependency of the amplitudes, which is given by the cosine of the radiation angle θ between propagation direction and vertical axis z. A relation between the decreasing amplitude with an increasing distance r to the source is given by the spherical spreading factor, which is also proportional to the value of $(\frac{1}{vr})^{1/2}$ for the 2-D wave propagation. Certain phase and frequency parameters are a characteristic of the wavelet and these parameters must be restored for the waveform resulting from the summation. An amplitude spectrum proportional to the square root of frequency (f) for 2-D migration and a 45-degree constant phase shift, form the wavelet shaping factor. To finally perform the summation method, the input data has to be multiplied by the obliquity factor and the spherical spreading factor, before restoring phase and frequency parameters. All this can also be derived from the scalar wave equation with P as the wave field and x, z as axes of the Cartesian coordinate system:

$$\Big(\frac{\delta^2}{\delta x^2} + \frac{\delta^2}{\delta z^2} - \frac{1}{v^2}\frac{\delta^2}{\delta t^2}\Big)P(x,z,t) = 0 \ , \tag{2.12}$$

and the Kirchhoff integral solution of the 2D scalar wave equation

$$P(x,z,t) = \frac{1}{4\pi}\int\Big[\ \overbrace{\frac{1}{r}\Big(\frac{\delta P}{\delta z}\Big)}^{vertical-gradient} + \overbrace{\frac{cos\theta}{r^2}P}^{near-field-term} + \overbrace{\frac{cos\theta}{vr}\frac{\delta}{\delta t}P}^{far-field-term}\ \Big] \ . \tag{2.13}$$

Equation 2.13 can be subdivided into three terms: the vertical-gradient term, near-field-term and the far-field-term. After all, only the far-field-term is the basis for the Kirchhoff migration, since the near-field-term describes the wavefield close to the source and the vertical-gradient-term depends on the z-derivative. The output wavefield is then respectively described by

$$P_{out} = \frac{\Delta x}{4\pi} \sum \frac{cos\theta}{vr} \frac{\delta}{\delta t} P_{in} \ . \tag{2.14}$$

The subsurface points are weighted, depending on the distance r from the source points (P_{in}) to the output wavefront (P_{out}). In the case of pre-stack migration, the Kirchhoff summation is done based on the nonzero-offset traveltimes. The Kirchhoff depth migration is using these equations to calculate the ray paths along the complete model, examine the seismic energy and summing up these amplitudes. The performance of the complete migration is done by migrating each shot independently and afterward stack the migrated shots to receive an image of the subsurface which is corrected for the effects of wave propagation.

Tomography of depth-migrated gathers

NMO correction and migration are both processes which update the data by removing time and wave effects from it, on the basis of a sufficient velocity model. Enhancing the velocity model is an iterative step which is needed to improve the data quality since not all unwanted effects can directly be removed. Furthermore, an initial interval velocity model is built on the relation of the Dix formula which is still an inaccurate determination of a complex interval velocity function due to its restriction to flat-layered media and to the lack of lateral velocity variations. The migration velocity analysis (MVA) method is an iterative process where the data is first depth-migrated and subsequently, the interval velocity model is updated on the basis of the migration results.

As an indication of the accuracy of the interval velocity model, the coherency of the image in the migrated common image gathers (CIG) is given. Different approaches depending on how the coherency is calculated, are available. In this case, only the coherency along the offset axes is measured and will be referred to as offset-domain CIGs (ODCIG). The flatness of the depth-migrated image gathers indicates how well the data was constrained by a good velocity model. If the velocity model was inaccurate, a residual moveout (non-flatness) on the CIG is observed and a residual moveout (RMO) analysis on the ODCIG can be performed. It can be distinguished between two different ways of migration velocity analysis. A first one is based on the simple relation of the Dix formula where the interval velocities are updated on the basis of the average velocity errors also referred to as the Deregowski loop. Limitations of the Deregowski loop can be found since it is only valid under the assumption that the reflector geometry is not too complex and that strong lateral velocity variations are absent. Furthermore, the interval velocities are updated in the vertical direction with the same corresponding horizontal location of the CIG. This approach has not been included in the MVA of this thesis since reflection tomography is the most favorable choice.

Reflection tomography of migrated data is the second method to perform MVA, and represents a global approach in comparison to the Deregowski loop, which considers the entire model and updates the shallow and deep sections at the same time. Applied on pre-stack depth-migrated data, tomography makes use of the residual depth error on the depth image gathers and an updated velocity-depth model can be achieved by calculating this residual moveout, z_{rmo}, as

follows:

$$z_{rmo} = z_{\rho 0}\left(\sqrt{1 + \frac{1-\rho^2}{\rho^2}\frac{|h|^2}{z_{\rho 0}^2}}\right)z \quad . \tag{2.15}$$

The RMO is given as a function of the absolute offset of the data $|h|$, with respect to the zero offset depth $z_{\rho 0}$. Additionally, ρ is described as the ratio of the true migration slowness to the current migration slowness and z is the unit vector in direction of depth. In practice, a first step in tomography connects the depth residual moveout to time because the non-flatness (Δt) indicates a time delay (Δt_i) between time at zero offset (t_0) and at a further offset. In principle, Δt_i is the result of an error in velocity (δV) and depth (δZ) and an equation needs to be built which relates all values (Equation 2.16):

$$\Delta t = \Sigma \Delta t_i \quad . \tag{2.16}$$

Equation 2.16 is written for each ray and solved using least squares to find the optimal values for the unknowns.
Commonly two different tomography methods exist: Horizon-Based Tomography and Grid-Based Tomography. Horizon-based tomography is a simple method which calculates the residual moveout, i.e. the error in depth as well as velocity, along predetermined horizons (Jones, 2010). Δt is derived by semblance analysis, where the semblance is first calculated along picked horizons and picked at maximum semblance values. The horizons are sampled on a predetermined interval of common reflection points (CRP). At these points, the velocity and horizon-depth are updated by the tomography.
In contrast to horizon-based tomography, only an error in velocity is assumed for grid-based tomography and the unknowns have to be solved for the complete section and not only from the horizons. Grid-based tomography is based on picked segments in the section where the RMO is calculated for. These segments are commonly auto-picked and reveal more subsurface structures than only the identified reflections for the horizon-based procedure. It is used in situations where it is difficult to select horizons and to refine velocity sections after horizon-based tomography has been applied.

CHAPTER 3

Processing of the Oc270 data

3.1 Introduction

The most important steps of seismic data processing that have been applied are discussed in this chapter in a structured manner. In this thesis, the seismic line Oc270_029 from cruise Oc270 on the R/V Oceanus was re-processed in the time domain, with the goal of enhancing the former results by Mountain and Monteverde (2012).
The raw data was analyzed using the freeware Seismic Unix (SU), primarily for editing the data headers. Next steps of pre-processing were done with the chosen software package ProMax from Halliburton/Landmark. After finishing these steps with a pre-stack migration in the time domain, the pre-stack depth migration can be finally performed with a Kirchhoff depth migration approach. For this, as well as for enhanced migration velocity analysis the Software GeoDepth by Paradigm was used.
In Figure 3.1 the processing workflow is presented. The processing steps were divided into pre-processing, velocity analysis in the time domain, time to depth conversion with the final pre-stack depth migration and reflection tomography.

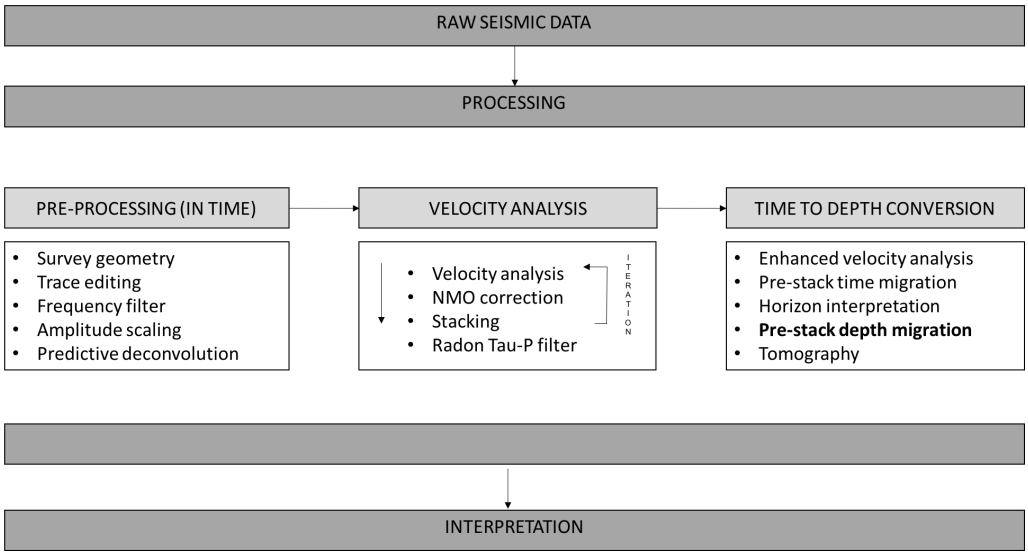

Figure 3.1: Workflow of the seismic data processing.

3.1.1 Raw Data

Survey Oc270 was conducted in June 1995 as part of the project: High-Resolution Seismic Surveying (Chief Scientist: Gregory Mountain). The raw data of line Oc270_029 was part of a seismic data grid which was acquired with the LDEO Portable HiRes Multi-Channel Seismic system. This line was compiled in a SEG-Y format and included multi-channel reflection seismic shot data which was acquired from southeast to northwest direction. The starting point of the line had the coordinates *39.310693 N, -73.050975 W* beginning at the New Jersey slope towards the less deep and more landward part of the New Jersey shelf, finishing the line at point *39.098157 N, -72.661347 W* (Figure 1.5). Marine seismic data was acquired by using an AirGun:GI45/45 as a source and a 48 channel streamer as a receiver of 600 m length. The distance from the source to the nearest channel was 34 m and the channel distance was 12.5 meters. The distance from the source to the antenna added up to 55 m. In contrast to the depth of the source which could vary between 1.2 and 2.7 meters, the depth of the receiver cable was fixed at 3 m. Recording of the seismic data took place with a sample interval of 500 microseconds and a record length of 3 seconds. Oc270_029 was acquired in a completely straight line with an overall length of around 42 km (Table 3.1).

Table 3.1: Acquisition parameters of the seismic survey line Oc270_029.

Profile length	42 km
Number of shots / channels	3264/48
Shot / channel interval	12.5/12.5 m
Sampling rate	0.5 ms
Recording length	3000 ms
CDP interval	6.25 m
Max. CDP fold	40

3.1.2 Header editing

The original SEG-Y file containing the seismic data of line Oc270_029, did not contain any geometry information in the header and so this had to be added manually. As well as the original raw data file, a shot navigation file was provided online by the Marine Geoscience Data System. The seismic shot point navigation data file *ts.n.029* contained information about the time, number, and coordinates of every single shot point. The navigation file made it possible to assign the geometry information to the source and receivers of the dataset. The shot coordinates had to be extracted from the navigation file and converted into the Universal Transverse Mercator (UTM) coordinate system. Manual checking of the navigation file and the SEG-Y file showed that more shots were counted in the naviagtion file (3288 shots) than in the raw data file (3264 shots). Acquired shots without any geometry information and the shot number had to be eliminated from the dataset: 1-4, 623, 890-891, 893-915, 3132. Overall 3259 shots were used. To assign the geometry of the seismic data, several source and receiver parameters were used: UTM coordinates, the number of channels, distance from the source to the first channel, group spacing and streamer azimuth (Appendix A.1 & A.2). They were created from the navigation file and then written in the SEG-Y trace headers.

3.2 Pre-stack processing with ProMAX

The commercial software package SeisSpace/ProMAX 2D (V5000.8.0.0) from Halliburton/Landmark was used for processing the data set. Throughout this thesis references towards this software is made by using the term of ProMAX. The processing was done on a HP ProDesk 600 G1 TWR running on the operating system openSUSE (release 13.2) for Linux 3.16.7. The hardware of this system was an Intel(R) Core(TM) i5-4590 CPU at 3.30 GHz.

Several pre-processing steps were applied to the offshore seismic data set from New Jersey shelf (Figure 3.1). The edited SEG-Y file was loaded into ProMAX resulting in the first raw shot. These data points were displayed as the present shot number with the containing channels against time. Figure 3.2 shows the acquired data of the 48 channels of the shots 104, 105 and 106 against the two-way travel time. It can be seen that the reflections are visible but masked by a significant amount of noise and several malfunctioning traces. Data will only be shown until 2000 ms two-way travel time in the time domain and until 2000 m for depth migration, as no primary seismic events are identifiable below. An Automatic Gain Control (AGC) was applied on the stacked section to increase the amplitude and to improve the visibility of late-arriving events. During the seismic survey, not all hydrophones recorded optimally and channels were dead while acquiring the data, and therefore had to be excluded. Despite the fact that dead traces occurred on different channels for every shot, the channels 6 and 25 appeared to be noisy within the complete dataset and therefore had to be excluded. Besides these, several other traces were killed after a quality check of the data and an overall amount of 68 dead traces were identified and removed from the data set.

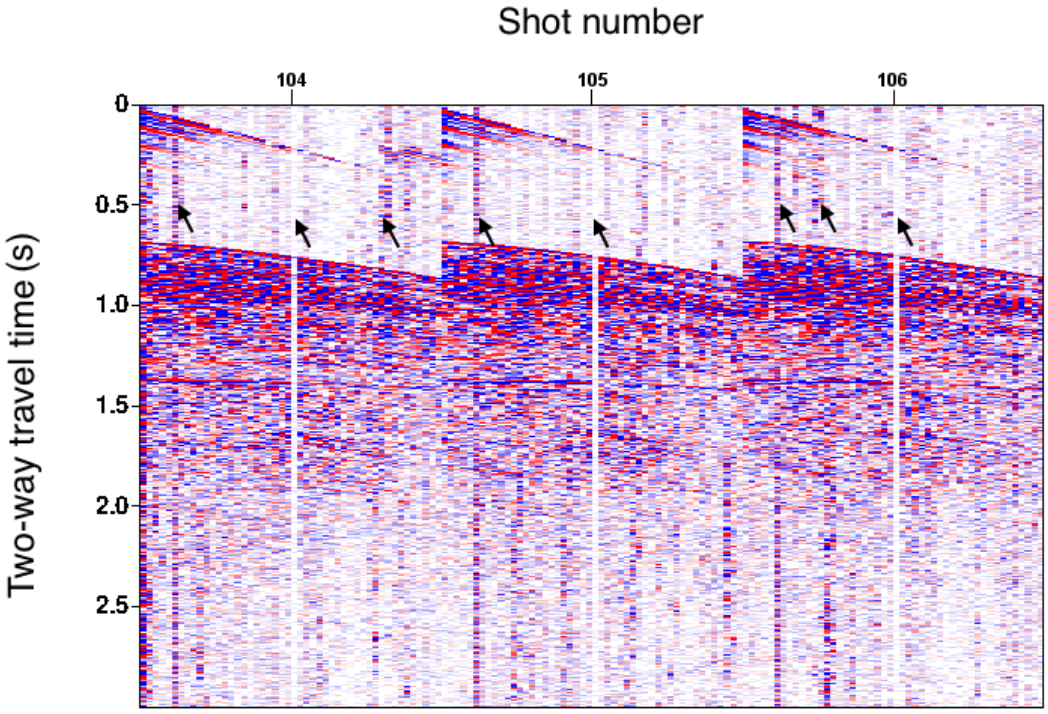

Figure 3.2: Unprocessed image of the raw data (shot 104, 105 and 106). Black arrows mark malfunctioning traces.

Frequency Filter

For the first application of a filter on the raw data, a zero-phase Ormsby bandpass filter was chosen. The zero-phase Ormsby bandpass filter was defined in two stages: first the low-cut was defined (4 & 8 Hz), followed by the high-cut (100 & 150 Hz) using several parameter tests where higher frequencies were tested, too. Chosen values for the single Ormsby bandpass filter were 4 - 8 - 100 - 150 Hz. A bandpass filter was applied to the data to reduce noise level and strengthen the useful frequencies.

Geometry

Since the geometry of the straight line Oc270_029 was relatively easy, the provided 2D marine geometry spreadsheet was used for the geometry structure. The most important task was to assign the CDPs. CDPs were defined ranging from 110 to 6719 with an offset bin center increment of 25. Following the completed geometry definition, the data was sorted into CDP gathers, which was necessary for subsequent NMO correction and stacking.

Normal Moveout Correction

To achieve a first stack of the data set, a NMO correction had to be applied. To be able to check the quality of the pre-processing steps this initial stack was defined with a simple starting velocity model (Appendix A.3). Since this initial velocity model was not optimal, NMO correction of the seismic data was not properly performed. This was a step which was iteratively improved. After CDP sorting and NMO correction were performed, the seismic data was stacked into a section. In Figure 3.3 the initial stack, so-called Brute Stack, is displayed, showing first structures of the subsurface. The seismic image was far from being noise free, not all reflections were continuous yet and not every structure was resolved. Only structures until 1000 ms could be resolved and strong multiples e.g. at 300 ms and 500 ms still had to be filtered out. The waterbottom reflection was very well detectable. Additionally, the occurrence of a data gap between CDP 1933 and 1964 was visible.

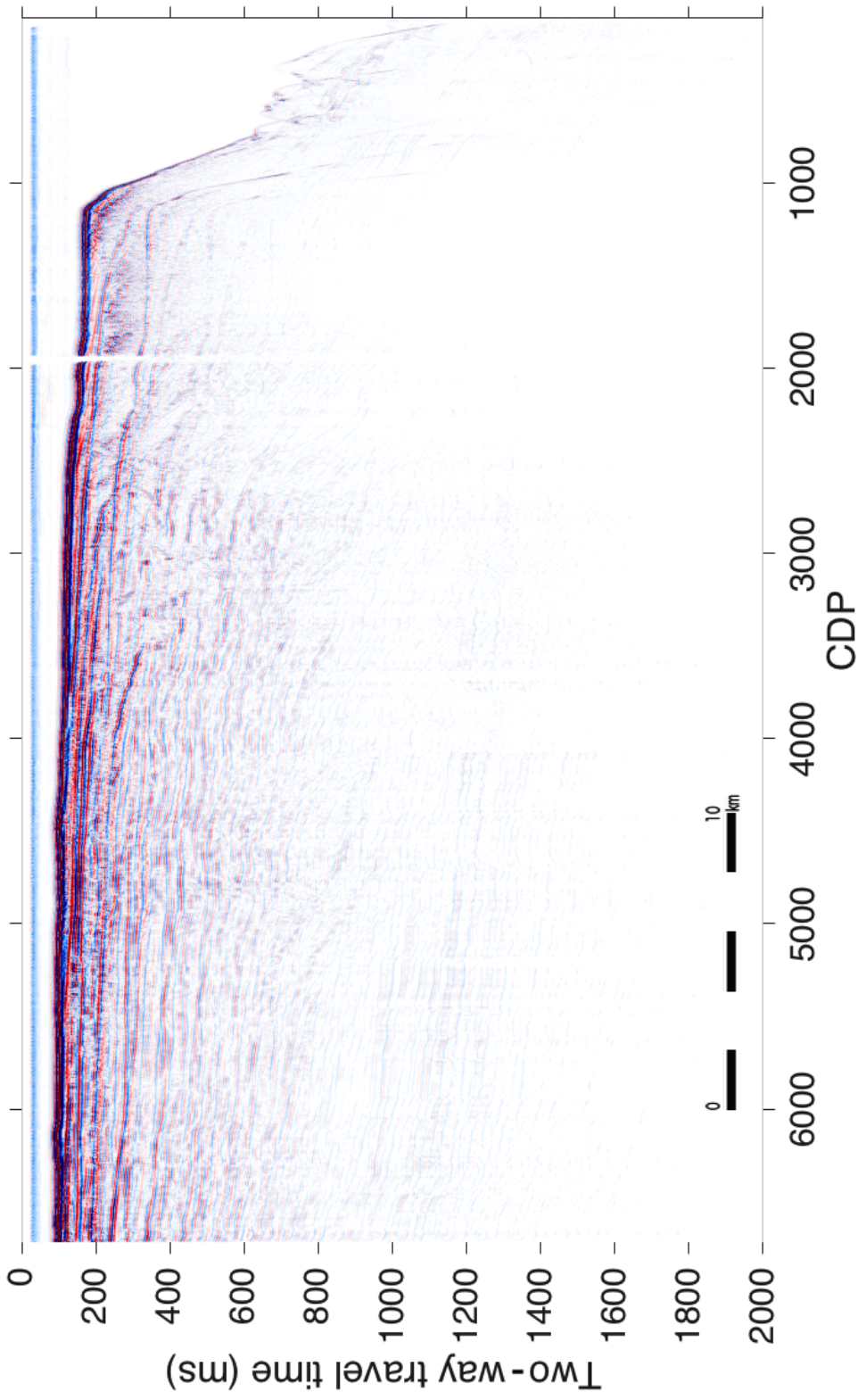

Figure 3.3: Initial stack of the raw data with a single 4 - 8 - 100 - 150 Hz Ormbsby bandbass filter applied.

True Amplitude Recovery

To solve Equation 2.6 a parameter test was performed for the exponential factor and the cut-off time. For the exponential factor n under the condition of $\frac{1}{distance}$, a range from 0 to 20 with increments of 1 was tested. The best result was found using $n = 3$. The cut-off time k corresponds to the maximum application time of the TAR. The maximum application time for the TAR was determined to be 2000 ms.
For the purpose of comparison, another stacked image was produced and displayed in Figure 3.4. The application of TAR to the seismic data had a significant effect. Primarily, the noise of the first break was reduced and reflections became more visible in the uppermost part of the image. It may be argued that TAR results in loss of too much information of the first arrivals, but on the other hand, amplitudes at later times were increased which result in a visibility of deep reflections. Especially structures which were not as clear became more visible and new dipping events were identified.

Predictive Deconvolution

To perform deconvolution, a deconvolution gate was required in ProMAX. The deconvolution gate was chosen to start just below the first breaks, hence deconvolution was only applied to the region below the deconvolution gate. In this case, a constant white noise level of 0.1 s was used. The prediction lag α and operator length n were checked for a certain range of values by more parameter tests. For the operator length n the following values were tested: 80 ms, 100 ms, 200 ms. 100 ms was determined to be the best operator length. A next parameter test was done for the prediction distance. The values the prediction distance were tested for are 6 ms, 10 ms, 20 ms and 40 ms. 20 ms was determined to give the best result.
The result of predictive deconvolution is shown in Figure 3.5. Compared to Figure 3.4, significant changes are marked by multi-colored arrows which are further explained within the figure itself. At a first impression, it seemed that the predictive deconvolution results in a loss of data, but it was actual to the contrary. As a result of the predictive deconvolution, noise and multiples were filtered out and only the real reflections became more visible.

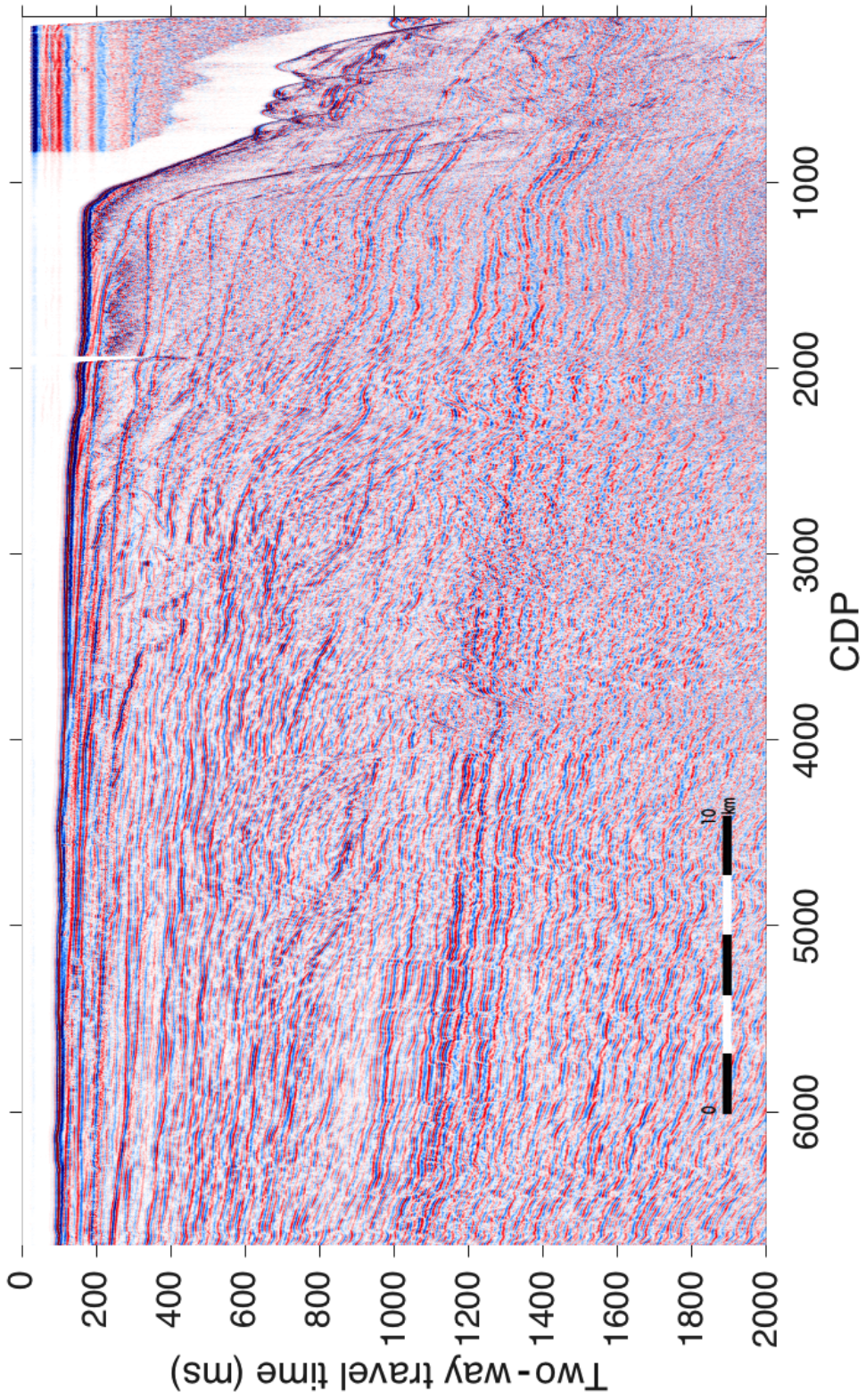

Figure 3.4: Stacked image after true amplitude recovery was applied.

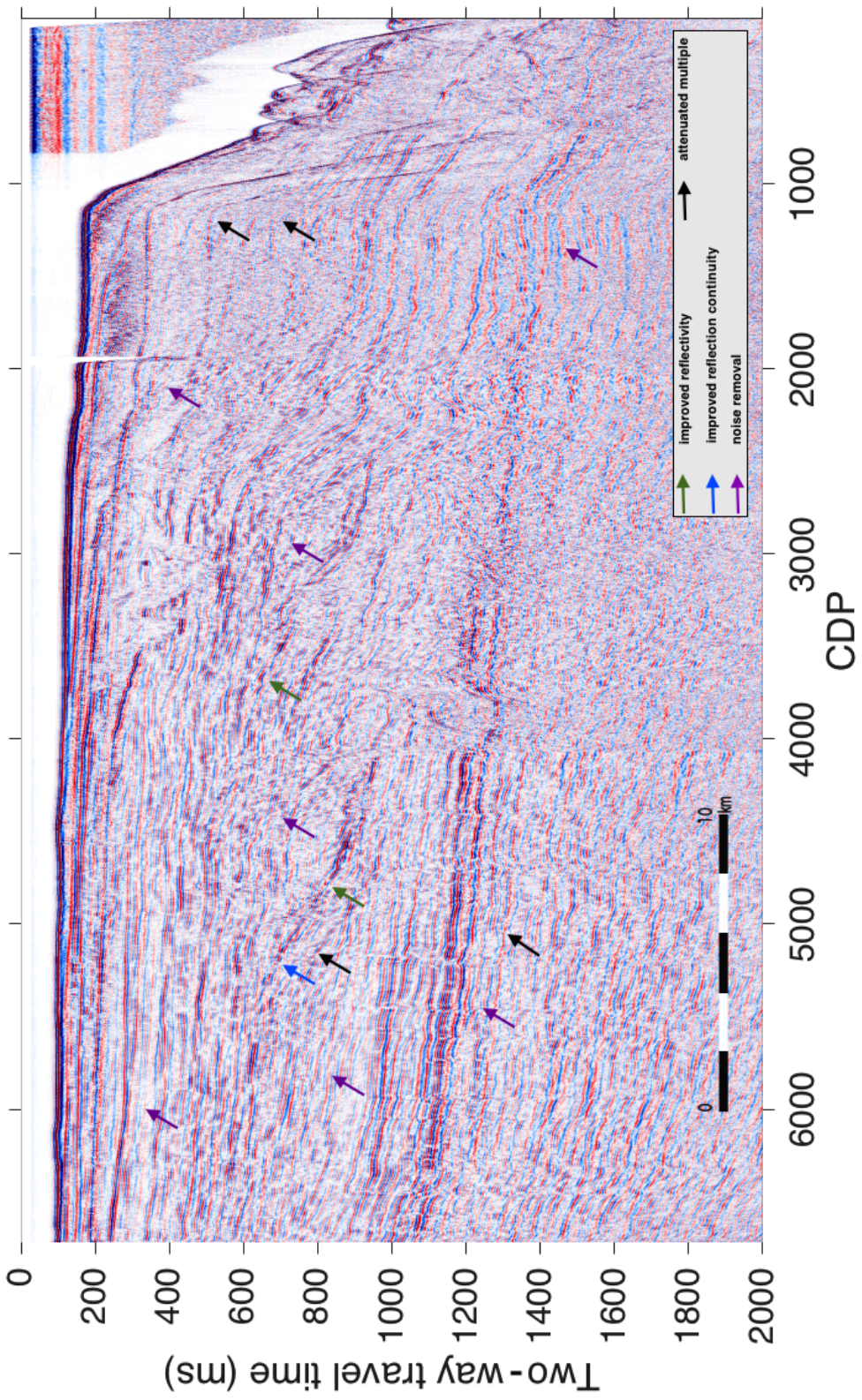

Figure 3.5: Stack after predictive deconvolution. Multi-colored arrows mark the areas of major changes based on the comparison to the stack after true amplitude recovery was applied (Figure 3.4).

Velocity Analysis

For determination of the rms velocity, a semblance analysis was performed on the supergathers, where each supergather comprised data of 3 CDPs. Semblance is a measure of coherency of the resulting stacked trace (after the application of NMO) as a function of various velocities. Maximum semblance values correspond to maximum coherency which were manually picked. The resulting rms velocity model was used for NMO-correction of the data to produce high-quality stacks.

An example of the semblance panel while picking of the rms velocities is represented in Figure 3.6. The semblance panel displayed the stack response as a function of the velocity and time in a contour plot (Yilmaz, 2001). In this figure, different regions with high semblances are displayed. The semblance maxima indicate the correct rms velocity for a reflection event at a certain two-way travel time.

For the velocity analysis, 21 CDPs were analyzed with an increment between the CDPs of 300. After the initial velocity analysis (Figure 3.6) on the selected CDPs had been performed, a resulting velocity model was built along the complete profile. This model was still very crude and needed to be improved further. After three iterations of repeated velocity picking, on the same CDPs chosen earlier, a final velocity model was produced. The final velocity model is shown in Figure 3.7 and it can be seen that the velocity increases with depth, which is the expected behavior in a sedimentary environment. Together with the velocity model, an updated stack is displayed in Figure 3.8. Compared to the initial stacked section (Figure 3.5), it was clear that a precise velocity model improves the image significantly. Since velocities were picked more frequently than for the initial stacks, more information was added (purple arrows) and multiples were attenuated (black arrows), especially in areas where the signal-to-noise ratio was low. Furthermore, it strengthened the main reflection continuity (blue arrows) and emphasized new structures and dipping events by an improved reflectivity (green arrows).

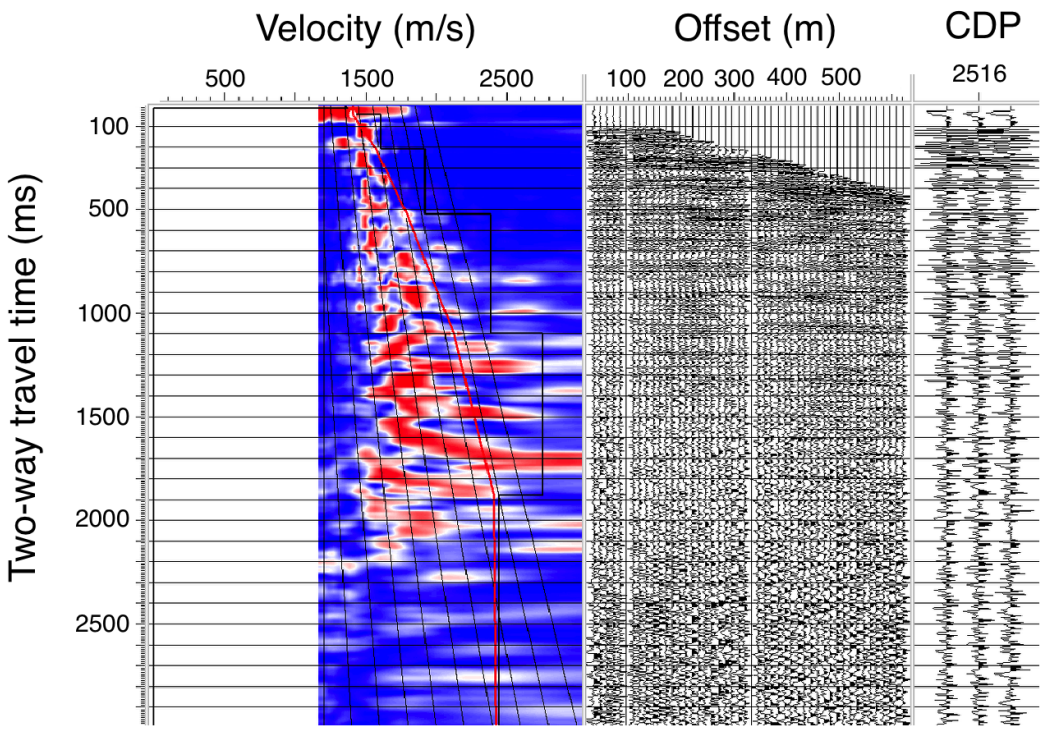

Figure 3.6: Velocity analysis for CDP 2515. Velocities are picked in the semblance plot for reflecting events. The semblance panel displays the stack response as a function of TWT and the velocity in a contour plot (left). Maximum semblance values which correspond to maximum coherency are displayed in red color.

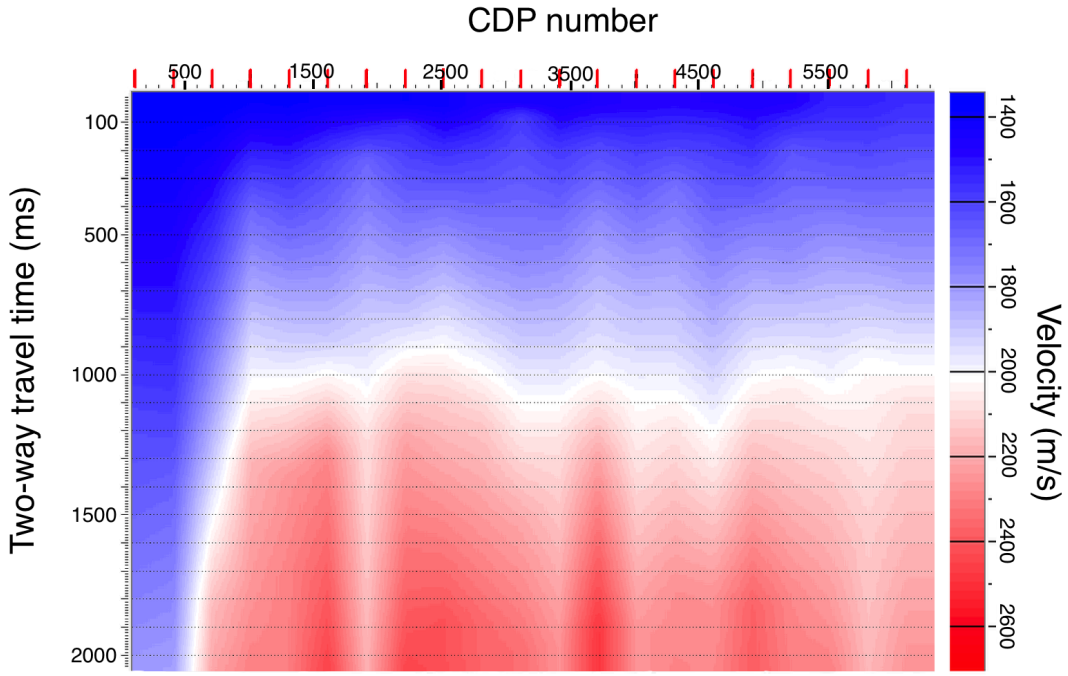

Figure 3.7: The final velocity model was built after picking velocities on 21 CDPs along the complete profile with a CDP increment of 300. CDPs increase from left to right.

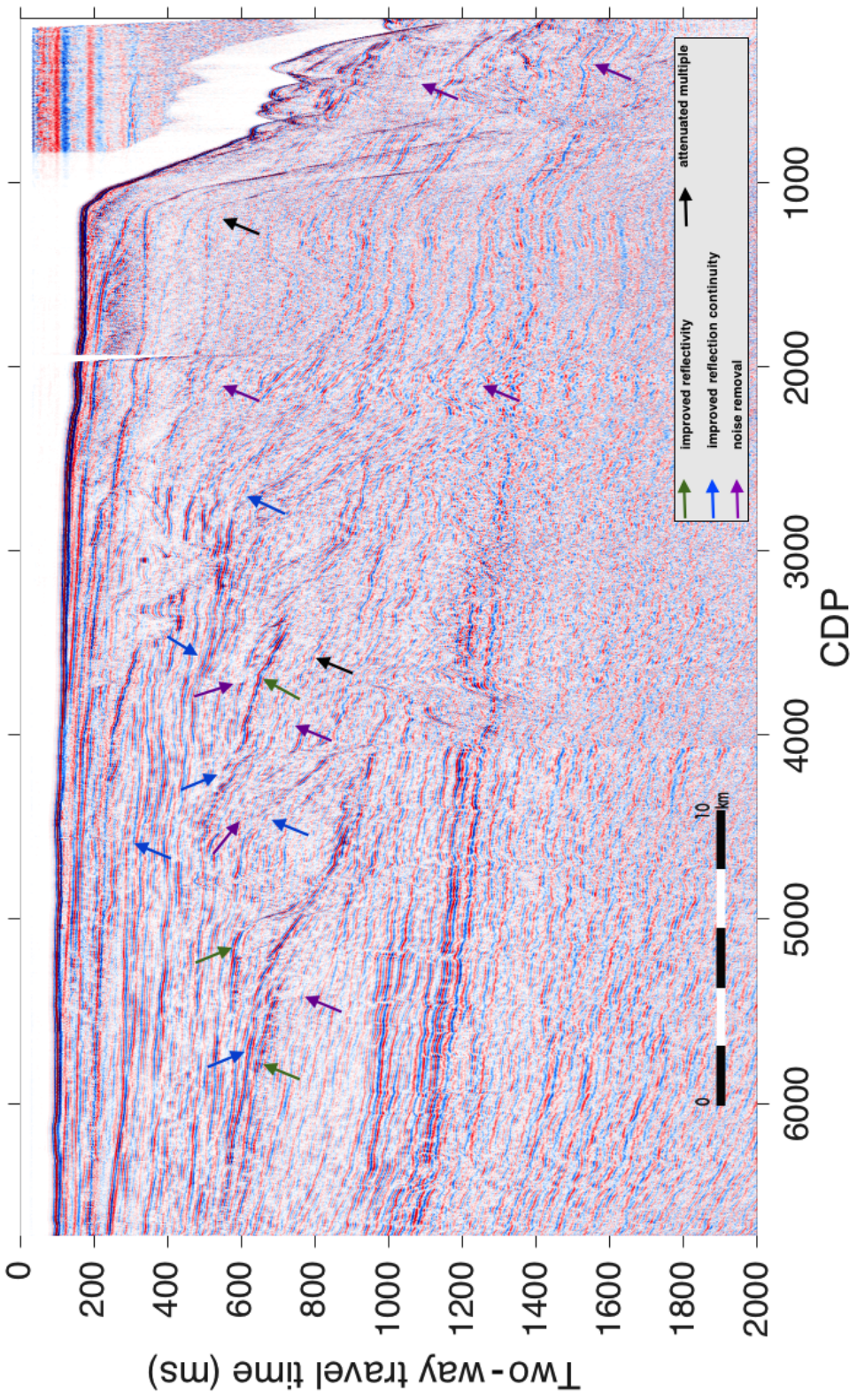

Figure 3.8: Stacked image after the enhanced velocity analysis was applied. Multi-colored arrows mark the areas of major changes compared to the previous stack displayed in Figure 3.5.

Radon Filter

Most multiples were filtered out or attenuated during pre-processing steps described above however, some strong multiples, like at 300 ms, were still slightly visible (Figure 3.8). The Radon filter weakened these remaining multiples very successfully. To achieve this, a specific bottom mute was picked and applied in the Radon domain (Figure 3.9). Picking the bottom mute was the final step of the Randon analysis where the data was diplayed as RMO versus time. It was possible to distinguish between primaries and multiples since primary reflections were set to zero residual moveout and multiples were not mapped to zero residual moveout in the Radon domain. The bottom mute was applied in a way that the effect of the multiples were substracted from the data. Even after performing all these processing parameters it was not possible to completely suppress these multiples. Image improvement was achieved in the earlier times until 500 ms. The part between CDP 5270-6719 in the time range of 500-700 ms was inferior to that improvement.
The application of the Radon filter extended the data gap between CDP 1933 and 1964 all the way down to 2000 ms. It was already visible in the previously stacked images, that within this area the image is not as clear as the surrounding. The blurry area was extinguished after the $\tau - P$ transformation had been performed.
Multiple attenuations by the Radon filter completed the pre-processing stage and the obtained data set could be exported as a new SEG-Y file for further use.

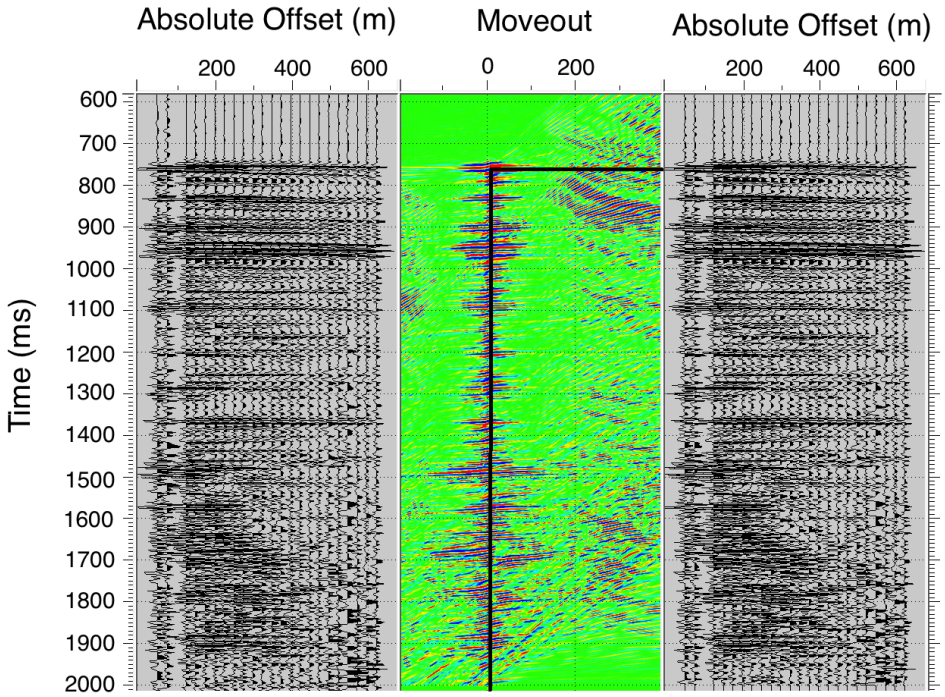

Figure 3.9: Bottom mute applied on the seismic data set. Boundary of the bottom mute is marked by a black line in the central $\tau - P$ panel. The panel to the left is showing the t-x input while the filtered t-x panel is given in the most right panel.

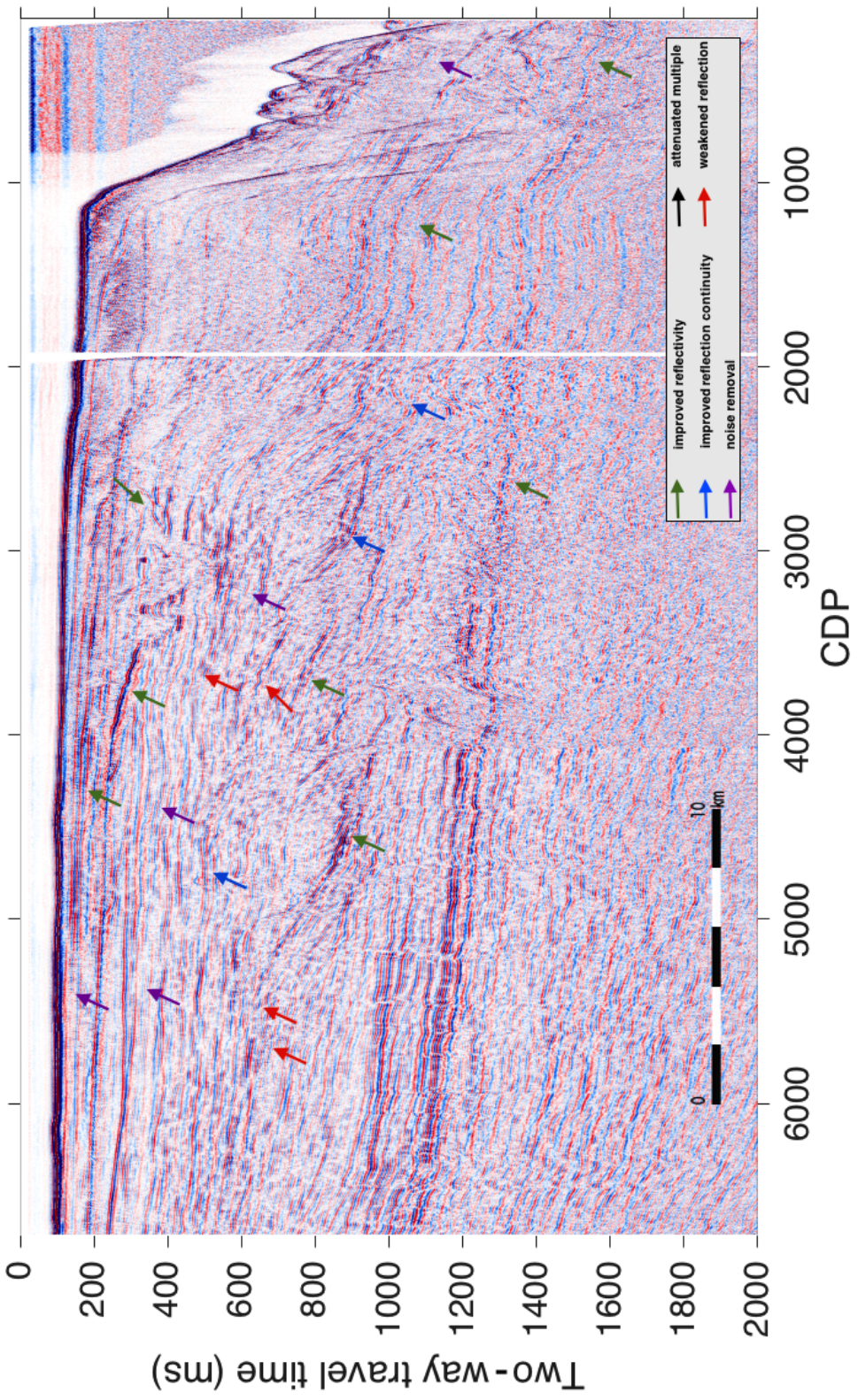

Figure 3.10: Stack after Radon transform with multi-colored arrows that mark the areas of major changes compared to the stacked image (Figure 3.5), of the previous processing step.

3.3 Kirchhoff Pre-stack Depth Migration

After finalizing the pre-processing of the data in the time domain, the objective was to migrate the seismic data and to convert it into the depth domain. This was performed by a different software called GeoDepth, established by Paradigm.
It was proceeded with the unmigrated output after the radon transformation. Due to the change of software, a new rms velocity model had to be designed for the migration process considering that the previous model could not be transferred. A rms velocity model with a CDP gather increment of 100 was built and rms velocities were picked. In practice, the velocity picking was identical to the procedure described in Section 3.2. Semblance panels were created and maximum values were picked within these velocity semblances. On the basis of the newly defined rms velocity model, a Kirchhoff pre-stack time migration algorithm was executed (Figure 3.11). The time-migrated stacked section was useful for quality control of the data, but the most important application was to identify horizons. Horizons were picked due to their reflector continuity and intensity, with no specific intention of matching with geological interpretations or sequence stratigraphy. Overall, seven horizons were defined for the procedure of the depth migration, displayed in Figure 3.11. These horizons were needed to evaluate the interval velocities between the identified reflections for the initial interval velocity model used for Kirchhoff depth migration.

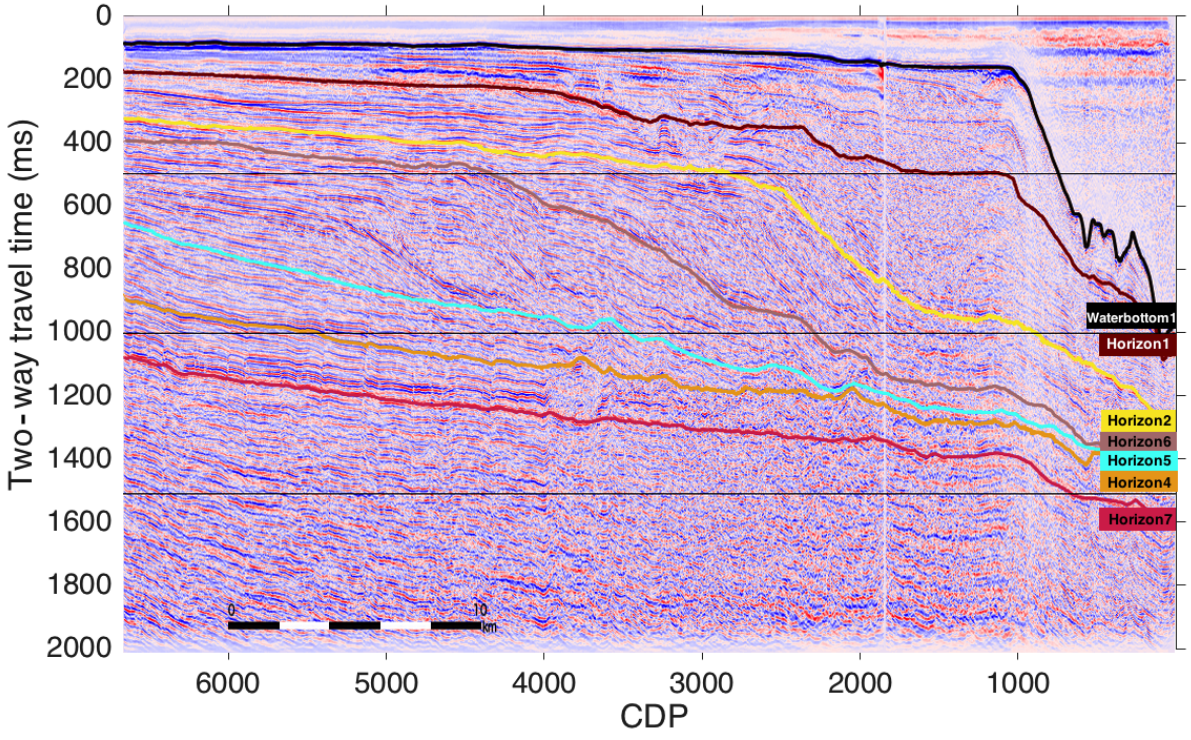

Figure 3.11: Pre-stacked time-migrated image including the seven interpreted horizons: (1) Watterbottom1 - black, (2) Horizon1 - red, (3) Horizon2 - yellow, (4) Horizon6 - brown, (5) Horizon4 - blue, (6) Horizon5 - orange, (7) Horizon7 - pink.

Before it was possible to migrate time horizons to depth, an interval velocity analysis was required. The initial interval velocity model was calculated on the basis of the available rms velocity function. An example of a velocity semblance of such an interval velocity analysis is given in Figure 3.12 from the first horizon (Waterbottom1).
It was a layer stripping process which worked in different stages. For receiving a range of velocities, the picked horizon on the time-migrated model needed to be demigrated. Evaluated interval velocities were picked and defined for the first upper horizon along the profile. Afterward, the time model was ray-migrated to the depth and the depth structure for this first horizon was defined. Completing these steps for the first horizon made it possible to continue with the second horizon and so on (Figure 3.13). This layer stripping process is necessary because the depth of the upper layer effected the velocity of the lower layer due to the relation of the Dix inversion and the layer-strip-off of the contributions from the layer above (Jones, 2010). All interval velocity information were gathered in a 2D horizon velocity model and an interval velocity section could be derived from it (Figure 3.14). Pre-stack depth migration could be performed on the basis of the created interval velocity section and the final depth-migrated section is displayed in Figure 3.15. A maximum application depth of 2000 m was determined.

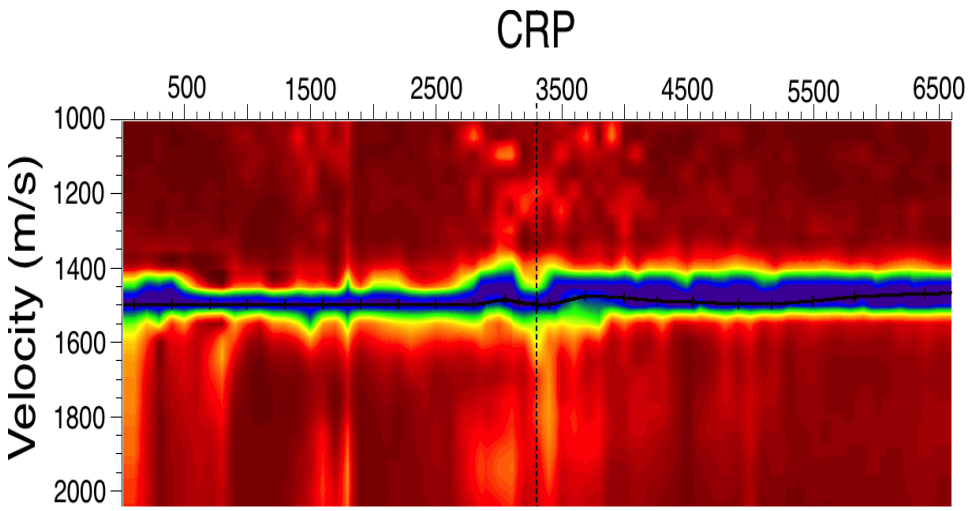

Figure 3.12: Example of a horizon interval velocity semblance from the Watterbottom1 horizon during velocity refinement. The CRPs are increasing from left to right. Dark blue color corresponds to maximum coherency while minimum coherency is displayed by dark red color. Oink numbers visible on the vertical axes gives the velocity values.

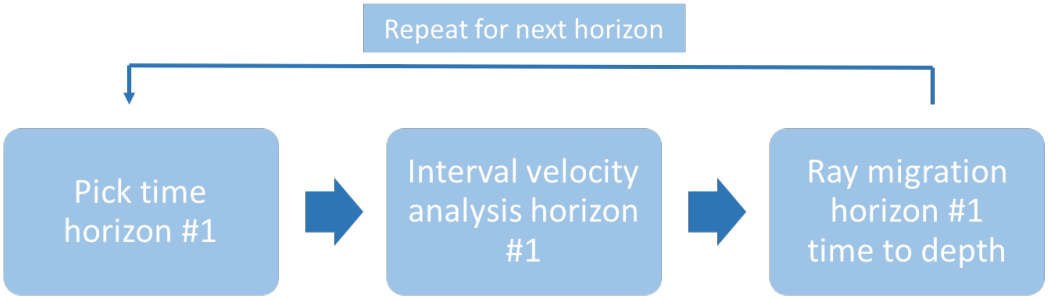

Figure 3.13: Steps performed during the layer stripping process for the individual horizons.

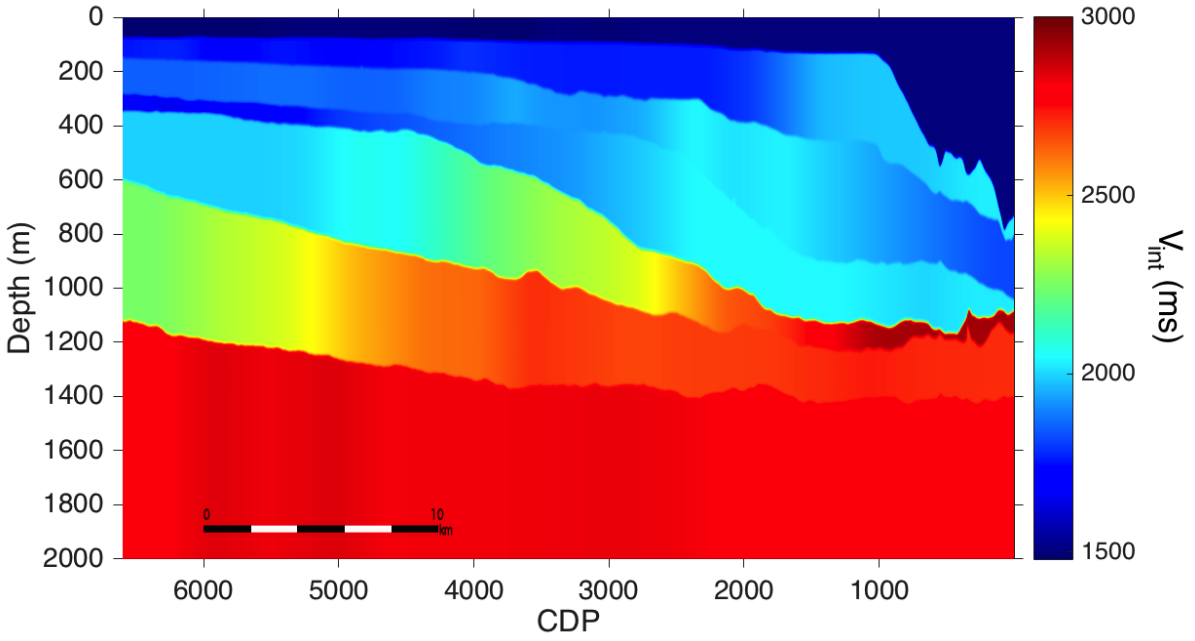

Figure 3.14: Interval velocity section from seismic profil line Oc270_029 derived for the initial pre-stack depth migration.

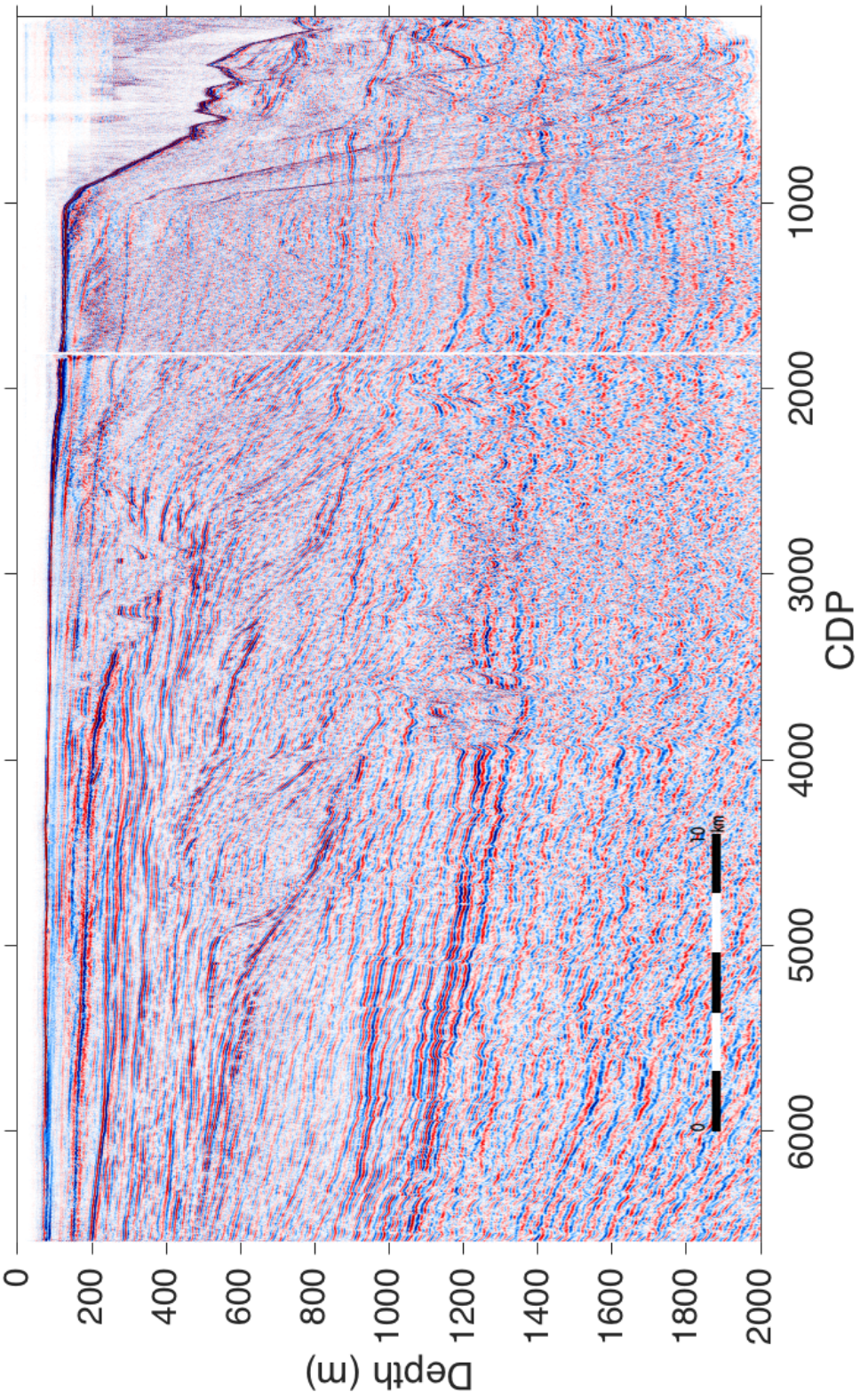

Figure 3.15: First pre-stack depth-migrated image displayed down to a depth of 2000 m.

3.4 Tomography

Horizon-Based Tomography

After performing the Kirchhoff pre-stack depth migration, examination of the migrated gathers revealed residual depth moveout. Then the RMO was further reduced by adjusting the velocity-depth model by applying reflection tomography.
The picked horizons (Figure 3.11) were used to perform the horizon-based depth tomography. Horizon interval velocity semblances were created to update the interval velocities for each horizon by refining the picking of the horizon interval velocities (Figure 3.16). These interval velocity analyses were similar to rms velocity analyses but they differ in the way the moveout curves were calculated. In this case a non-hyperbolic moveout by zero offset ray migration and CDP ray tracing though the model was predicted. The offset of the depth-migrated gathers was chosen as the input data. Interval velocity refinement used the curved ray migrated gathers and the initial interval velocity model as the input data set. The error in velocity was analyzed based on the degree of non-flatness in the gathers. These analyses were performed manually on a range of CDP locations along the horizons with a CDP increment of 200 CDPs. Concluding the enhanced interval velocity picking, a new interval velocity model was built which automatically updated the initial velocity model. Additionally, an updated velocity section was created from the new model.
Figure 3.17 shows the improved velocity section before performing again the Kirchhoff pre-stack depth migration with the new interval velocity section (Appendix A.1). It also describes the effect of the tomography on the interval velocity model for areas of major changes in lateral velocity as well as in the updated depth of the horizons itself. Since the improved velocity section had such an influence on the migrated image, these changes were also visible on the updated stacked depth-migrated image (Figure 3.18). Especially the shift of the reflection depth due to the tomography was visible on the migrated section as well. Depth gathers became flatter, which indicated the positive effect of this tomography approach.

Grid-Based Tomography

Even after performing the horizon-based tomography, a slight non-flatness was observed in the depth image gathers. A last step of interval velocity refinement was the grid-based tomography. On the base of the last depth-migrated section, 2D tomography segments were created (Figure 3.19), using the built-in auto-picker. The model, as well as the picked segments, were used as an input additionally to the depth image gathers. As before, a maximum application depth of 2000 m was implemented.
The choice of the grid resolution made a great difference in the outcome. It had to be defined in x (CRPs) - and in z (m) -direction. A high resolution of 50 CRPs times 100 m led to satisfying results. For CRP ray tracing calculations, a value of 3 CRPs was chosen to still produce reliable results with adequate processing time.
Since a velocity model was available, a choice could be made which layers the tomography should be performed in. It was also possible to use a constant update to all grid points that were located within the boundaries of a specific layer. In this case, the first layer i.e. the

waterbottom, and the last layer were not included.
The grid-based tomography created an updated velocity section and also led to an improvement in the horizon-depth. In contrast to the earlier interval velocity sections, the updated model exhibited many lateral and small-scale variations (Figure 3.20). The last Kirchhoff pre-stack depth migration was performed leading to a good result. Main effects of the applied tomography on the migrated section in respect to the previous migrated image are shown in Figure 3.21.

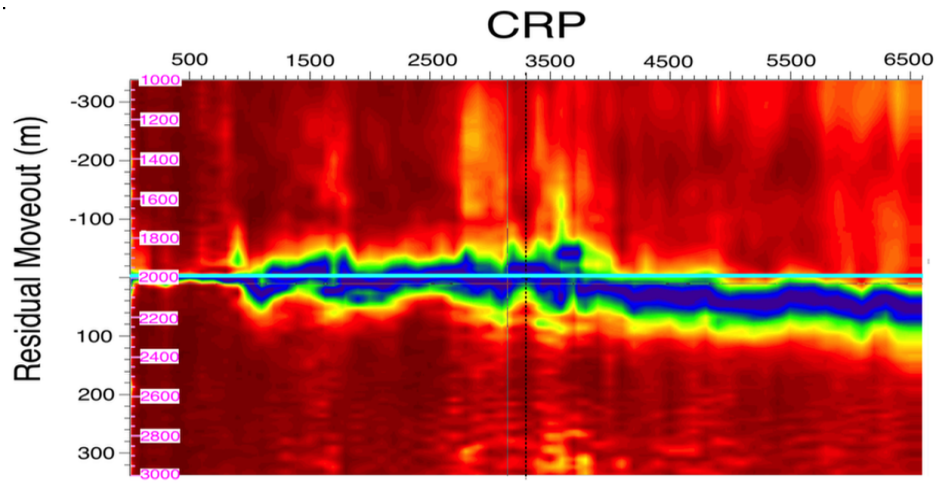

Figure 3.16: Example of a horizon velocity semblance from the Watterbottom1 horizon. The central light blue line indicates zero residual move out. Dark blue color corresponds to maximum coherency while minimum coherency is displayed by dark red color. CRPs are increasinf from left to right.

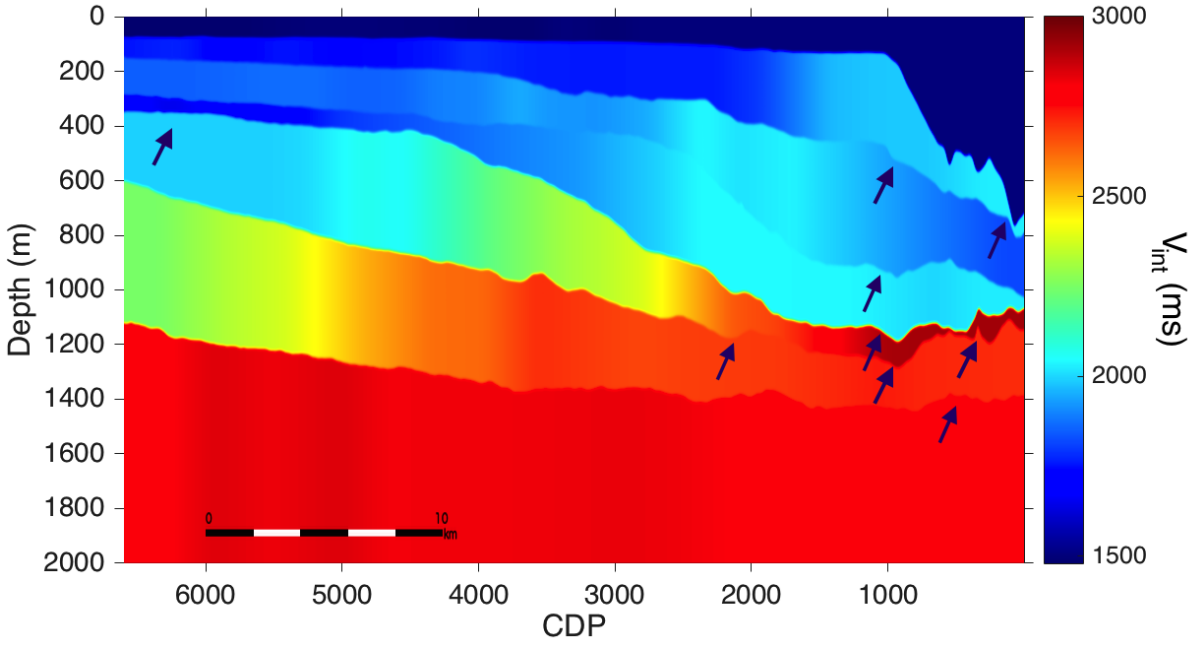

Figure 3.17: Refined interval velocity section after horizon-based tomography derived for the pre-stack depth migration of seismic profile line Oc270_029. The blue arrows highlight areas of significant changes in the lateral velocity and the horizon depth with respect to Figure 3.14.

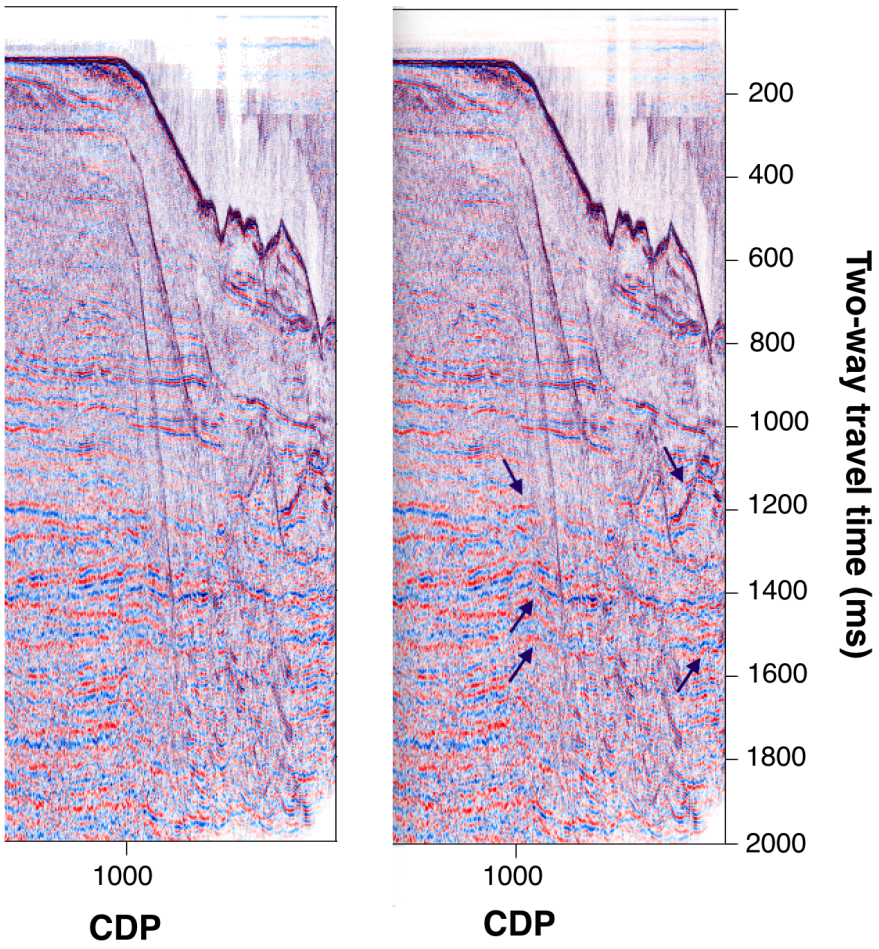

Figure 3.18: Comparison between the initial depth-migrated stacked image (on the left side) and the updated depth-migrated stacked image after horizon-based tomography (on the right side). Blue arrows mark the areas of significant changes, mostly due to an updated horizon depth.

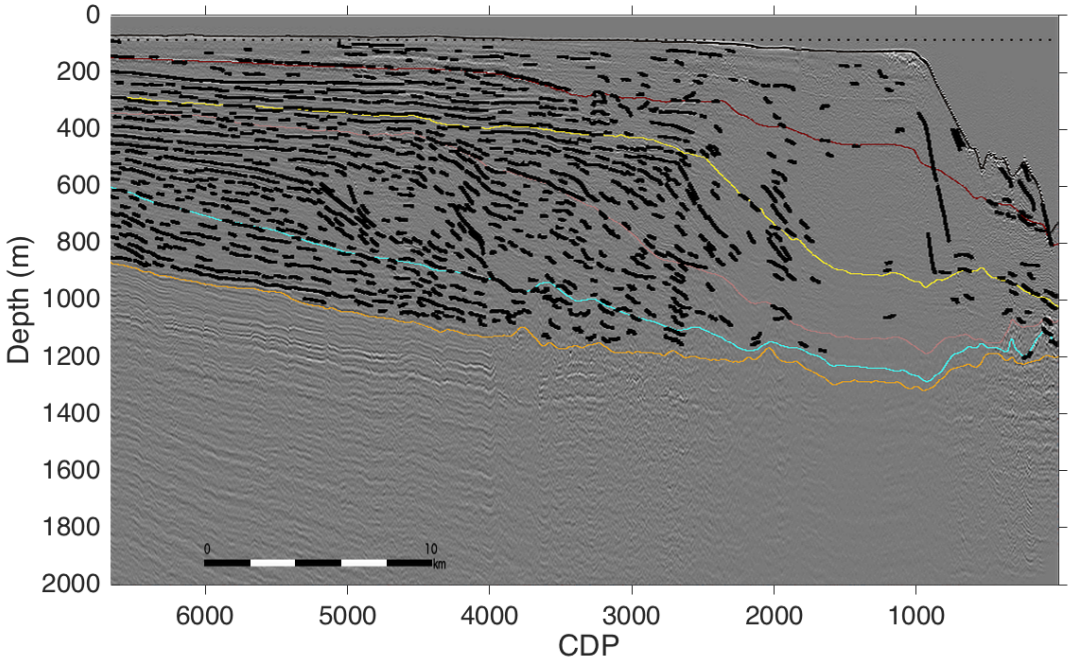

Figure 3.19: Identified segments for the grid-based tomography approach of seismic line Oc270_029. Segments were identified by auto-picking between the first horizon, (Waterbottom1) and Horizon4.

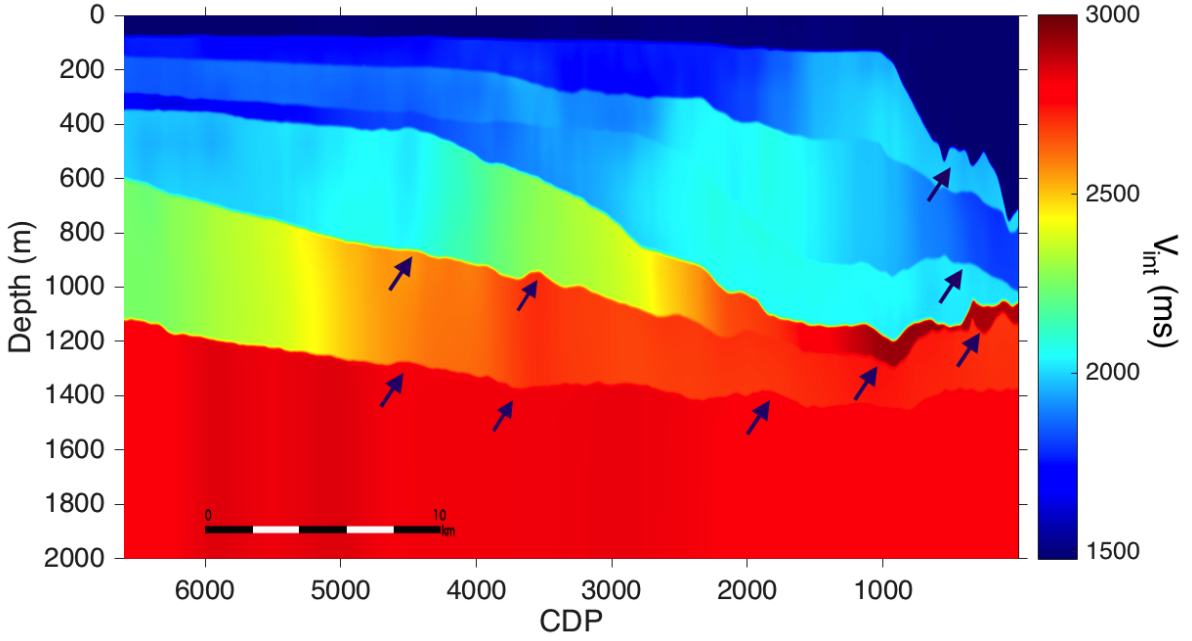

Figure 3.20: Refined interval velocity section after grid-based tomography derived for the pre-stack depth migration of seismic profil line Oc270_029. Changes with respect to Figure 3.17 are indicated by blue arrows.

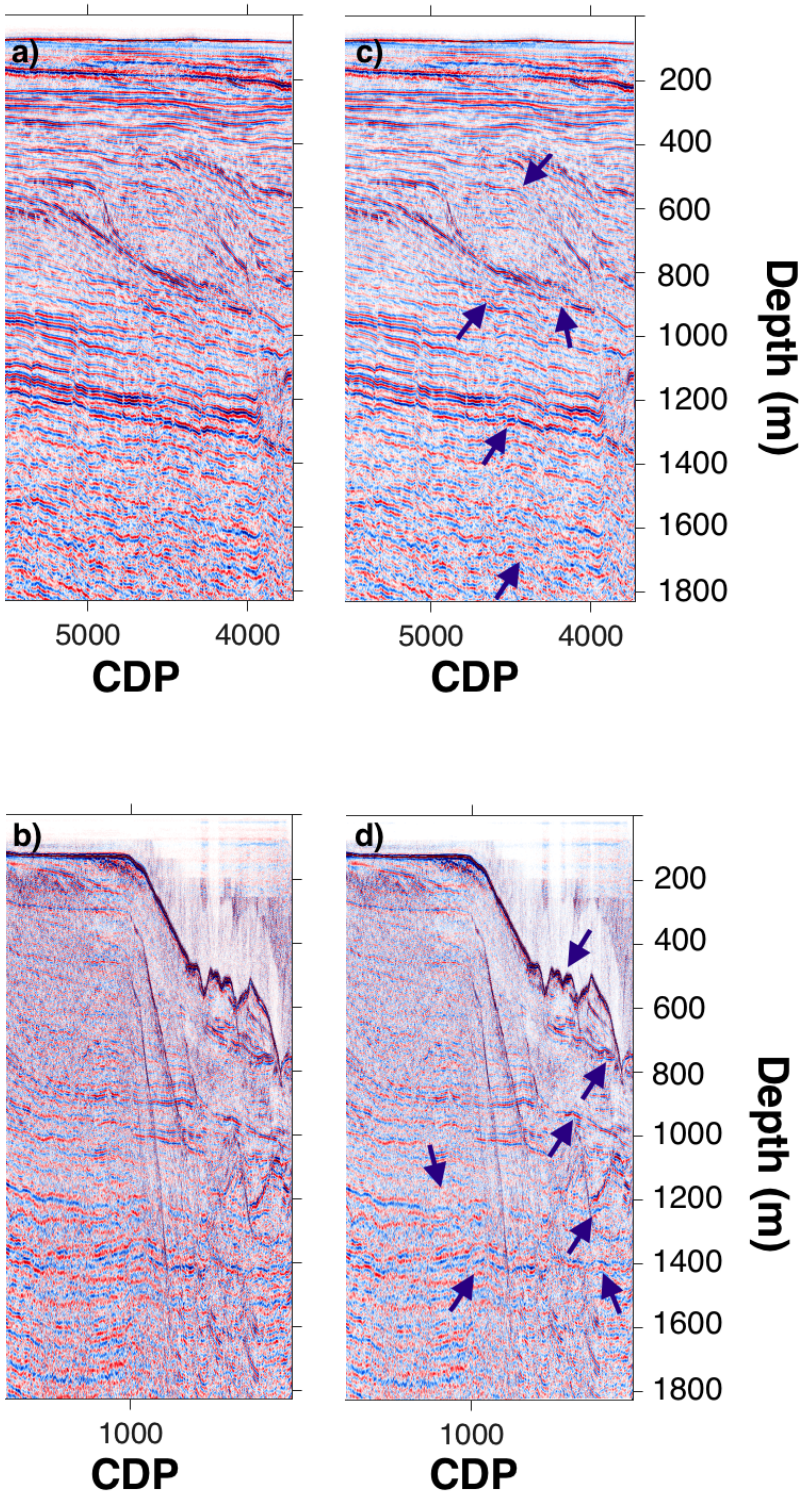

Figure 3.21: Comparison between the depth-migrated stacked image after horizon-based tomography was applied (a+b) and the updated depth-migrated stacked image after grid-based tomography (c+d). Blue arrows mark the areas of significant changes. Note that the depth of the zoomed in subfigures is not representing the complete depth.

CHAPTER 4

Interpretation and Discussion

Results achieved by this thesis can be devided into two parts. First of all, the outcome of the pre-processing was a time-migrated image. Since the seismic line Oc270_029 had been time-migrated before, the objective was to create an improved stack. Comparing the latest result of the time-migrated section by Austin et al. (1996) (Figure 4.1) with the improved time-migrated stack of profile Oc270_029 obtained in this thesis (Figure 4.2) demonstrated that the quality of the time-migrated image was improved. Improvement in the reflector continuity and the signal-to-noise ratio was achieved. Moreover, an increased amount of multiples were attenuated, enhancing the image of the important structures. Several strong reflections were visible and could be distinguished from the remaining attenuated multiples. The strong reflections at 600 ms and 1100 ms were especially traceable along the complete profile. An enhanced signal-to-noise ratio made it possible to identify structural events in detail. Between CDPs 3000 to 4000 in the time interval from 200 ms to 400 ms, an entire new dipping bed was visible. Additionally, the area close to the subsurface (down to 200 ms) was highly improved due to noise reduction. The improved time-migrated stack laid a better foundation for the ensuing time-depth conversion since distinctive horizons were identified within the section. More horizons were visible due to the improved reflector continuity and a better signal-to-noise ratio. As the quality of the horizons was improved, a better interval velocity model was built, due to the fact that the interval velocities were calculated along these horizons.

Since the main objective of the thesis was to apply seismic depth imaging to the data set acquired at the NJ shelf, it was proceeded accordingly. Figure 4.3 shows the final result after seismic depth imaging with applied tomography. Due to the conversion from time to depth, reflectors were moved to their true location in space below the seafloor and the shape of the subsurface features was truly revealed. Some inclined structures which were already visible in the time-migrated section became steeper in the landward part of the profile line, while the reflections at the slope revealed smaller dips. Those areas are marked by yellow rectangles in Figure 4.3. Especially the reflector continuity changed within the area of the slope. Reflectors became clearer and the intensity improved even under such a complex geology. Several small structures were identified within the migrated images, and since these structures are visible in the pre-stack time-migrated image (Figure 4.2) as well as in the post-stack time-migrated image by Austin et al. (1996) (Figure 4.1), and in the final depth-migrated stack (Figure 4.3) they can be considered as being real subsurface structures and no false artifacts induced by seismic processing.

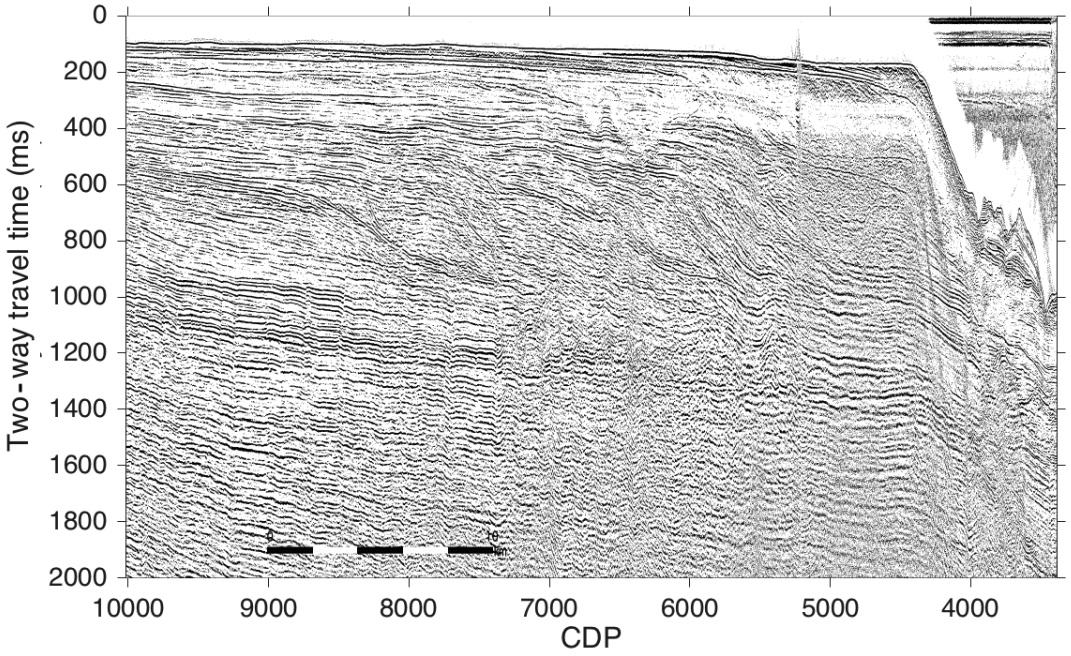

Figure 4.1: Post-stack time-migrated image of seismic line Oc270_029 by Austin et al. (1996). CDP numbers were assigned differently in comparison to the stacked images processed during this thesis, since it was initially processed as a continuation of the profile Oc270_129 and not as an independent seisimic profile.

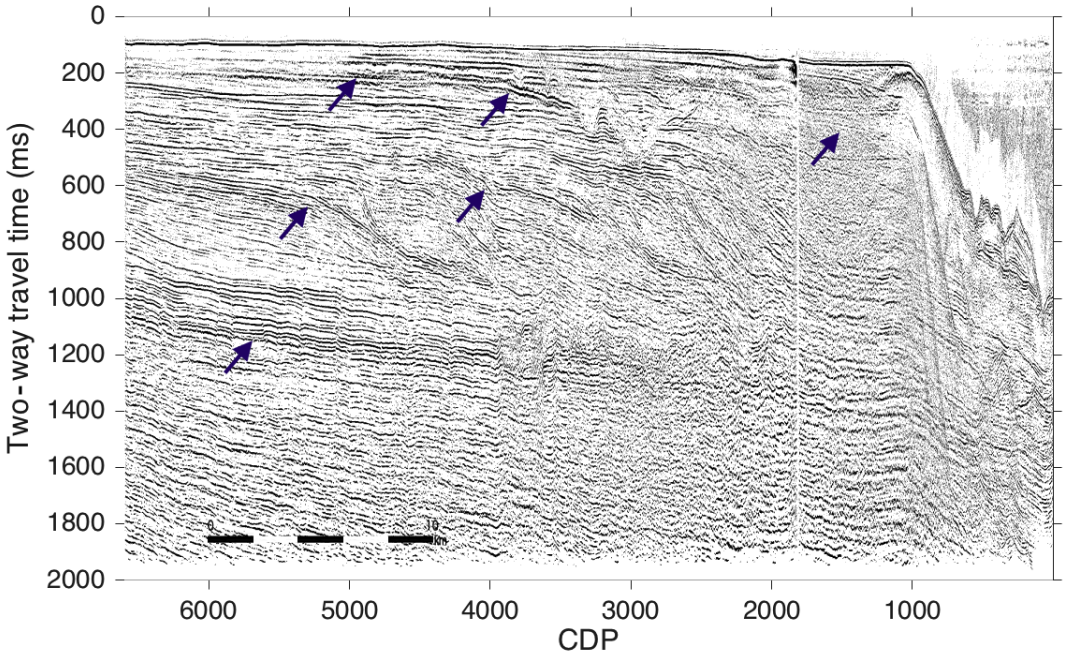

Figure 4.2: Pre-stack time-migrated image of the seismic profile line Oc270_029. Blue arrows mark areas of improvement compared to the post-stack time-migrated image by (Austin et al., 1996).

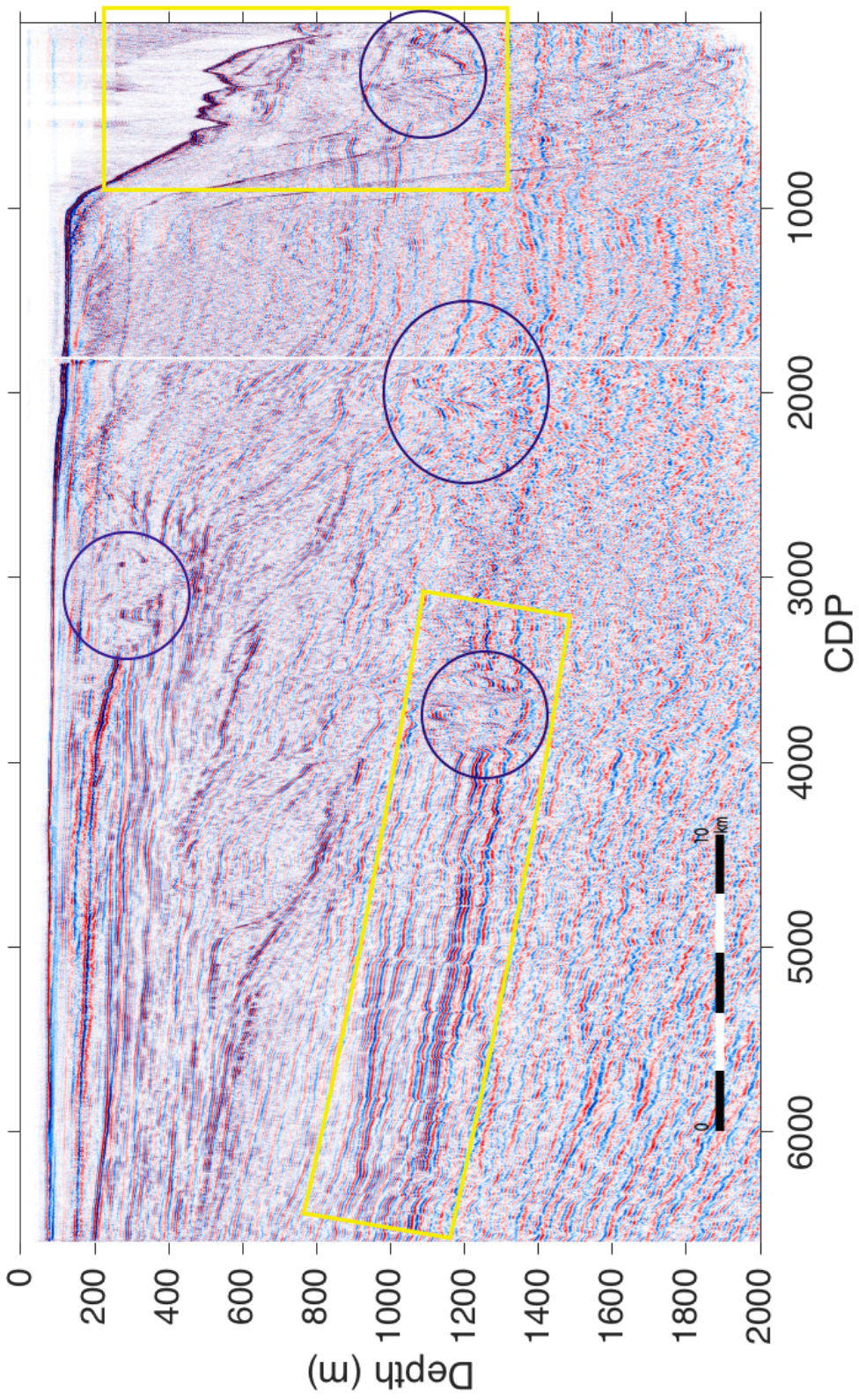

Figure 4.3: Stacked image of the depth-migrated section after interval velocity refinement was applied by a horizon-based tomography and a grid-based tomography approach. Yellow rectangles display the main changes of the reflector shape caused by time-depth conversion. Several structures are identified within the stack (blue circles).

Application of tomography led to a refinement in the depth migrated gathers and the remaining residual moveout was removed; especially the grid-based tomography improved the image by creating small scale changes in the interval velocity model. The depth-migrated seismic section provided the enhanced image of the subsurface which was used for further comparison and evaluation. It was very important to create the interval velocity model to build a reliable depth-migrated stack and it also gave a first insight into the subsurface structure along this profile, since different geological layers correspond to a specific velocity.
The depth-migrated stack showed seven prominent reflectors between 150 m and 1400 m which could be tracked along the complete profile and several smaller ones (Figure 4.3). However, the reflections at 200 m, 450 m, 850 m, 1000 m and 1050 m around CDP 6700 were the most outstanding ones. Profile Oc270_029 was acquired as the extension of the profile Oc270_529, and by comparison with the depth migrated section of Oc270_529, these five reflectors were also most prominent there and could be traced. Line Oc270_529 had already been interpreted in detail and it would have been good to proceed with the interpretation on line Oc270_029, too. Identified geological horizons and sequences from line Oc270_529 were confirmed by the borehole data, measured during IODP Leg 313 in the three boreholes M27, M28 and M29, with the help of a simplified 1D velocity model which was used to obtain a depth migrated image (Mountain and Monteverde, 2012; Miller et al., 2013a). A 15 km long gap between these two seismic profiles made it impossible to adopt the identified geological horizons from Oc270_529 for Oc270_029 directly, even when a continuation could be assumed. Available 2D seismic data sets in this area helped to fill this gap between the two seismic profile lines to continue with the geological interpretation. Figure 4.4 shows these four 2D-seismic lines (Oc270_129, Oc270_229, Oc270_329 and Oc270_429) which connects line Oc270_029 to Oc270_529, where each line is indicated by a different color along the combined profile Oc270 '29'.
Geological interpretations have been initially performed on the post-stack time-migrated stack of seismic line Oc270_529. Plotting all seismic post-stack time-migrated profiles of line Oc270 '29', which are online-avaiable, on each other in a line made it possible to trace the identified refectors from line Oc270_529 along the subsequent profiles until line Oc270_029 (Figure 4.4). Afterwards, these traced reflectors were transferred to the corresponding reflectors on the pre-stack time-migrated image. The knowledge, which reflectors of the profile line Oc270_529 correspondeed to the ones of Oc270_029 on the time-migrated stack gave an indication, where these reflectors were located on the depth migrated image (Figure 4.5).
Overall 4 sequences could be interpreted following the description provided by Miller et al. (2013a): Horizon *m1*, horizon *m4*, horizon *m5* and horizon *m5.2*. Another strong reflector at 300 m depth around CDP 6700 could also be traced up to the end of profile Oc270_529 but it had not been interpreted before. This reflector given by the purple horizon in Figure 4.5 is encountering the border to Oc270_129 at 450 ms and ends on profile Oc270_529 at 100 ms. Due to this transferable interpretation, it was possible to identify the corresponding time marker for four of the five identified sequences (*m1, m4, m5 and m5.2*) after Miller et al. (2013a) (Table 4.1).

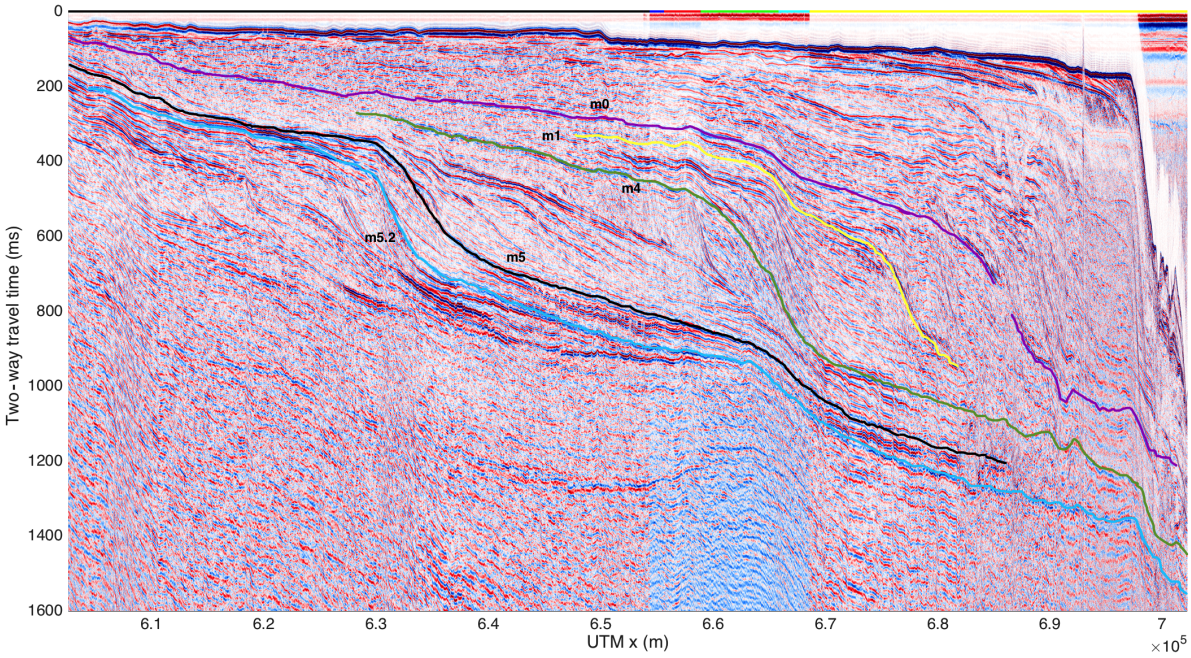

Figure 4.4: Combined seismic post-stack time-migrated sections of Oc270_029, Oc270_129, Oc270_229, Oc270_329, Oc270_429 and Oc270_529 with identified sequences by Miller et al. (2013a). Five sequences (*m1, m4, m5 and m5.2*) were traced up to Oc270_029 and were interpreted.

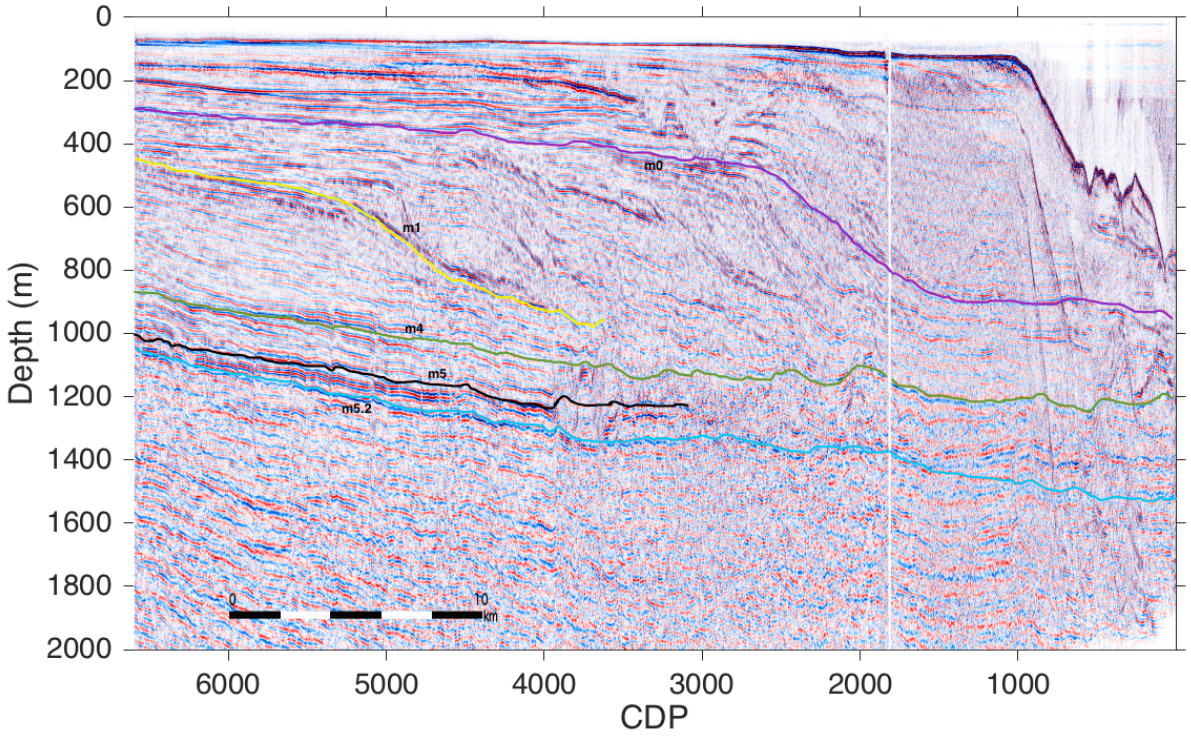

Figure 4.5: Interpreted horizons on the pre-stack depth-migrated image of seismic profile line Oc270_029.

Table 4.1: Determined age (Ma) of the identified sequences m1, m4, m5 and m5.2 after Miller et al. (2013a).

Sequence	**Age**
m1	11.6 - 11.8 Ma
m4	12.4 - 12.6 Ma
m5	13.7 - 14.8 Ma
m5.2	15 - 15.6 Ma

A pre-stack depth migration is very sensitive to changes in the interval velocity model which could also be observed during this thesis. Since small changes in the interval velocity model directly led to changes in the depth-migrated stack, this velocity model also gave evidence of the reliability of the pre-stack depth-migrated section. The method used for reflector interpretation of profile Oc270_029 was similar to the one used to gain more knowledge about the reliabiltiy of the interval velocity model. The processing workflow with the final Kirchhoff depth migration was initially established and applied at TU Bergakademie Freiberg for the seismic profile Oc270_529. An obtained interval velocity section of this profile was verified by the comparison with the data acquired of the discrete samples P-wave logger, deployed during IODP expedition Leg 313 (Appendix A.2 & A.2). A good consistency was achieved especially for the four identified layers *m1*, *m4*, *m5* and *m5.2* with only a small error between 1.5 m and 3.5 m (Riedel et al., 2016a), which is reasonable in terms of the resolution received while acquiring the seismic data. Considering again the gap between the two newly processed seismic profiles, it was not possible to maintain a direct comparison between the interval velocities, but the trend of fitting transition could definitely be observed. Plotting both velocity sections to each other made this trend even more obvious and assured the accuracy of the created interval velocity section for profile Oc270_029 (Appendix A.4). A consequence of the correct interval velocity model is the good reliability of the pre-stack depth migration performed during this thesis. Reliability of the interval velocity model is especially given in the upper 1200 m which is also the depth interval which is most influential to the deliverable groundwater flow simulations.
The applied processing workflow with the resulting depth migration produced a reliable outcome on the basis of an enhanced time-migrated stack. In comparison with the processing steps performed for the initial post-stack time migration of profile Oc270_029 several changes in the processing flow led to an improved image. Initial processing steps applied by Austin et al. (1996) were: mute, normal moveout correction, deconvolution and Stolt migration. Applying additional processing steps like the true amplitude recovery and radon transformation removed much noise and more multiples were attenuated. Furthermore, the Kirchhoff migration approach seems superior to the Stolt migration approach which does not encounter any lateral velocity changes.

CHAPTER 5

Conclusion and Outlook

Conclusion

In this thesis the reflection seismic profile Oc270_029 was migrated with the help of the Kirchhoff pre-stack migration approach in the time and depth domain. This included editing of the headers and pre-processing of the seismic data set while following a proposed processing workflow initially applied by Riedel et al. (2016b).
A pre-stack depth-migrated image of the subsurface along the seismic profile line Oc270_029 from the NJ shelf was produced on the basis of an improved pre-stack time-migrated stack. The reliability of the migrated section was confirmed by the comparison of the interval velocity sections of profile Oc270_529 and Oc270_029, comprising logging data from the IODP expedition Leg 313. Interpretation of four predefined sequences was possible by tracing the identified reflectors along several seismic profile lines (Oc270_529, Oc270_429, Oc270_329, Oc270_229, Oc270_129, Oc270_029). For the first time the proposed processing workflow developed at TU Bergakademie Freiberg (Riedel et al., 2016b) was applied for a seismic profile of the NJ data set different from the Oc270_529 profile. Overall, a high-resolution depth-migrated section was obtained in this thesis, which assured that the recommended processing flow is powerful for handling the NJ seismic lines, leading to a good result.

Outlook

Even when the applied processing flow led to sufficient results, further multiple attenuation is needed to remove the remaining multiples. The implementation of the surface-related multiple elimination (SRME,) developed at TU Delft (Verschuur et al., 1992), would be highly considerable due to the good results achieved in different marine seismic studies.
By tracing and transferring the identified reflectors to the depth migrated section of profile Oc270_029 it was possible to recognize several sequences within the image, nevertheless, it was by far not possible to trace all sequences interpreted by Miller et al. (2013a). To obtain all the desired information and to receive the true depth of the reflectors along the profile processed in this thesis, the four seismic data sets Oc270_129, Oc270_229, Oc270_329 and Oc270_429 have to be processed and depth-migrated to close the data gap. Furthermore, closing the gap can help to additionally confirm that the created velocity model represents the true subsurface velocities. If all horizons could be interpreted correctly along the profile Oc270 '29' a geological

interpretation of the sequence stratigraphy could follow.
To receive a 3D subsurface model, more profile lines of the NJ shelf have to be processed and interpreted. By applying the predetermined processing flow refined during this thesis, processing and computation time can be reduced.

List of Figures

List of Tables

Bibliography

J. Austin, C. Fulthorpe, G. Mountain, D. Orange, and M. Field. Continental-margin seismic stratigraphy: assessing the preservation potential of heterogeneous geologic processes operating on continental shelves and slopes. *OCEANOGRAPHY-WASHINGTON DC-OCEANOGRAPHY SOCIETY-*, 9:173–177, 1996.

B. L. Biondi. *Concepts and Applications in 3D Seismic Imaging.* Society Of Exploration Geophysicists, 2009.

R. Castelao, O. Schofield, S. Glenn, R. Chant, and J. Kohut. Cross-shelf transport of freshwater on the new jersey shelf. *Journal of Geophysical Research: Oceans*, 113(C7), 2008.

B. A. Christensen, C. Alexander, J. A. Goff, R. J. Turner, and J. A. Austin. The last glacial: Insights from continuous coring on the new jersey continental shelf. *Marine Geology*, 335: 78–99, 2013.

D. Cohen, M. Person, P. Wang, C. W. Gable, D. Hutchinson, A. Marksamer, B. Dugan, H. Kooi, K. Groen, D. Lizarralde, et al. Origin and extent of fresh paleowaters on the atlantic continental shelf, usa. *Ground Water*, 48(1):143–158, 2010.

G. Draaikoningen, E. Slob, and R. Ghose. Methods of exploration geophysics. *Lecture Notes AES1501*, pages 24–28, 2013.

S. Greenlee, F. Schroeder, and P. Vail. Seismic stratigraphic and geohistory analysis of tertiary strata from the continental shelf off new jersey: calculation of eustatic fluctuations from stratigraphic data. *The Atlantic Continental Margin. Geol. Soc. Am., Geol. of North Am. Ser*, pages 437–444, 1988.

S. M. Greenlee. Recognition and interpretation of depositional sequences and calculation of sea-level changes from stratigraphic data—offshore new jersey and alabama tertiary. 1988.

S. M. Greenlee, W. J. Devlin, K. G. Miller, G. S. Mountain, and P. B. Flemings. Integrated sequence stratigraphy of neogene deposits, new jersey continental shelf and slope: comparison with the exxon model. *Geological Society of America Bulletin*, 104(11):1403–1411, 1992.

J. C. Hathaway, C. W. Poag, P. C. Valentine, F. T. Manheim, F. A. Kohout, M. H. Bothner, R. E. Miller, D. M. Schultz, and D. A. Sangrey. Us geological survey core drilling on the atlantic shelf. *Science*, 206(4418):515–527, 1979.

C. Hübscher and K. Gohl. Reflection/refraction seismology. *Encyclopedia of Marine Geosciences*, 2014.

I. F. Jones. *An introduction to: Velocity model building*. Eage Publications, 2010.

M. A. Kominz, W. A. Van Sickel, K. G. Miller, and J. V. Browning. Sea-level estimates for the latest 100 million years: One-dimensional backstripping of onshore new jersey boreholes. In *Sequence Stratigraphic Models for Exploration and Production: Evolving Methodology, Emerging Models and Application Case Histories: Proceedings, 22nd Annual GCSSEPM Foundation Bob F. Perkins Research Conference*, pages 303–315, 2002.

H. Kooi and J. Groen. Offshore continuation of coastal groundwater systems; predictions using sharp-interface approximations and variable-density flow modelling. *Journal of Hydrology*, 246(1):19–35, 2001.

J. Lofi, J. Inwood, J.-N. Proust, D. H. Monteverde, D. Loggia, C. Basile, H. Otsuka, T. Hayashi, S. Stadler, M. J. Mottl, et al. Fresh-water and salt-water distribution in passive margin sediments: Insights from integrated ocean drilling program expedition 313 on the new jersey margin. *Geosphere*, 9(4):1009–1024, 2013.

W. Lowrie. *Fundamentals of geophysics*. Cambridge university press, 2007.

S. D. McAuley, J. L. Barringer, G. N. Paulachok, J. S. Clark, and O. S. Zapecza. Groundwater flow and quality in the atlantic city 800 foot sand, new jersey. 2001.

K. Miller and G. Mountain. Global sea-level change and the new jersey margin. In *Proceedings of the Ocean Drilling Program. Initial reports*, volume 150, pages 11–19. Ocean Drilling Program, 1994.

K. G. Miller, J. V. Browning, G. S. Mountain, M. A. Bassetti, D. Monteverde, M. E. Katz, J. Inwood, J. Lofi, and J.-N. Proust. Sequence boundaries are impedance contrasts: Core-seismic-log integration of oligocene–miocene sequences, new jersey shallow shelf. *Geosphere*, 9(5):1257–1285, 2013a.

K. G. Miller, G. S. Mountain, J. V. Browning, M. E. Katz, D. Monteverde, P. J. Sugarman, H. Ando, M. A. Bassetti, C. J. Bjerrum, D. Hodgson, et al. Testing sequence stratigraphic models by drilling miocene foresets on the new jersey shallow shelf. *Geosphere*, 9(5):1236–1256, 2013b.

K. G. Miller, J. V. Browning, G. S. Mountain, R. E. Sheridan, P. J. Sugarman, S. Glenn, and B. A. Christensen. History of continental shelf and slope sedimentation on the us middle atlantic margin. *Geological Society, London, Memoirs*, 41(1):21–34, 2014.

D. Monteverde, K. Miller, and G. S. Mountain. Correlation of offshore seismic profiles with onshore new jersey miocene sediments. *Sedimentary Geology*, 134(1):111–127, 2000.

D. H. Monteverde, G. S. Mountain, and K. G. Miller. Early miocene sequence development across the new jersey margin. *Basin Research*, 20(2):249–267, 2008.

G. Mountain and D. Monteverde. If you've got the time, we've got the depth: The importance of accurate core-seismic correlation. In *AGU Fall Meeting Abstracts*, volume 1, page 2111, 2012.

G. Mountain, J.-N. Proust, and the Expedition 313 Science Party. The new jersey margin scientific drilling project (iodp expedition 313): Untangling the record of global and local sea-level changes. *Scientific Drilling*, 10:26–34, 2010. doi: 10.5194/sd-10-26-2010. URL `http://www.sci-dril.net/10/26/2010/`.

C. W. Poag. Depositional history and stratigraphic reference section for central baltimore canyon trough. *Geologic Evolution of the United States Atlantic Margin: New York (Van Nostrand Reinhold)*, pages 217–263, 1985.

V. E. Post, J. Groen, H. Kooi, M. Person, S. Ge, and W. M. Edmunds. Offshore fresh groundwater reserves as a global phenomenon. *Nature*, 504(7478):71–78, 2013.

M. Riedel, S. Reiche, and S. Buske. Seismic depth imaging for fresh groundwater simulations at the new jersey shelf. *17th International Seismix Symposium*, P1.32, 2016a.

M. Riedel, S. Reiche, and S. Buske. A qualitative comparison of seismic imaging methods applied to data from the new jersey shelf. *76th Annual Meeting of the German Geophysical Society (DGG)*, Poster 6-L.009, 2016b.

E. A. Robinson and S. Treitel. *Geophysical signal analysis*, volume 263. Prentice-Hall New Jersey, 1980.

W. A. Schneider. Integral formulation for migration in two and three dimensions. *Geophysics*, 43(1):49–76, 1978.

D. W. Steeples. Shallow seismic methods. In *Hydrogeophysics*, pages 215–251. Springer, 2005.

M. T. Taner and F. Koehler. Velocity spectra-digital computer derivation applications of velocity functions. *Geophysics*, 34(6):859–881, 1969.

P. A. Toft and J. A. Sørensen. *The Radon transform-theory and implementation*. PhD thesis, Technical University of DenmarkDanmarks Tekniske Universitet, Department of Informatics and Mathematical ModelingInstitut for Informatik og Matematisk Modellering, 1996.

D. Trad. *Implementations and applications of the sparse Radon transform*. PhD thesis, University of British Columbia, 2001.

T. Ulrych and T. Matsuoka. The output of predictive deconvolution. *Geophysics*, 56:371–377, 1991.

R. van Geldern, T. Hayashi, M. E. Böttcher, M. J. Mottl, J. A. Barth, and S. Stadler. Stable isotope geochemistry of pore waters and marine sediments from the new jersey shelf: Methane formation and fluid origin. *Geosphere*, 9(1):96–112, 2013.

D. J. Verschuur, A. Berkhout, and C. Wapenaar. Adaptive surface-related multiple elimination. *Geophysics*, 57(9):1166–1177, 1992.

C. Wapenaar and A. Berkhout. *Advances in Exploration Geophysics*, volume 2nd. Elsevier B.V., 1st edition, 1989. ISBN 978-0-444-88472-5.

M. O. Withjack and R. W. Schlische. A review of tectonic events on the passive margin of eastern north america. In *Petroleum Systems of Divergent Continental Margin Basins: 25th Bob S. Perkins Research Conference, Gulf Coast Section of SEPM*, pages 203–235. SEPM, 2005.

M. O. Withjack, R. W. Schlische, and P. E. Olsen. Development of the passive margin of eastern north america: Mesozoic rifting, igneous activity, and breakup. *Regional Geology and Tectonics: Phanerozoic Rift Systems and Sedimentary Basins*, 1:301, 2012.

O. Yilmaz. *Seismic Data Analysis*. Society of Exploration Geophysicists, 2001.

APPENDIX A

Appendix

Table A.1: Original header entries of line Oc270_029

Name	**Oc270_029**
tracr	1 - 156528
fldr	1 - 3264
tracf	1 - 48
ep	1 - 3264
cdp	1 - 3264
cdpt	1 - 48
trid	1
duse	1
counit	1
ns	6000
dt	500
year	1995
day	180
hour	17 - 22

Table A.2: Added or changed header entries after editing of line Oc270_029

Name	**Description**	**Oc270_029**
sx	easting of source	7022082 - 6680886
sy	northing of source	43302948 - 43530312
gx	easting of receivers	7022361 - 6686025
gy	northing of receivers	43302752 - 43526816
gelev	elevation of receivers	-300
selev	elevation of source	-122
sdepth	source depth	122
scalel	scaling factor for elevation	-100
scalco	scaling factor for lateral coordinates	-10

Table A.3: Velocity function for Brute Stack.

Depth	**Velocity**
300	0-1480, 900-1650, 1100-1700, 1400-2000
400	0-1480, 800-1650, 1100-1700, 1300-2000
850	0-1480, 500-1650, 900-1700, 1200-2000
1600	0-1480, 400-1650, 700-1700, 1000-2000

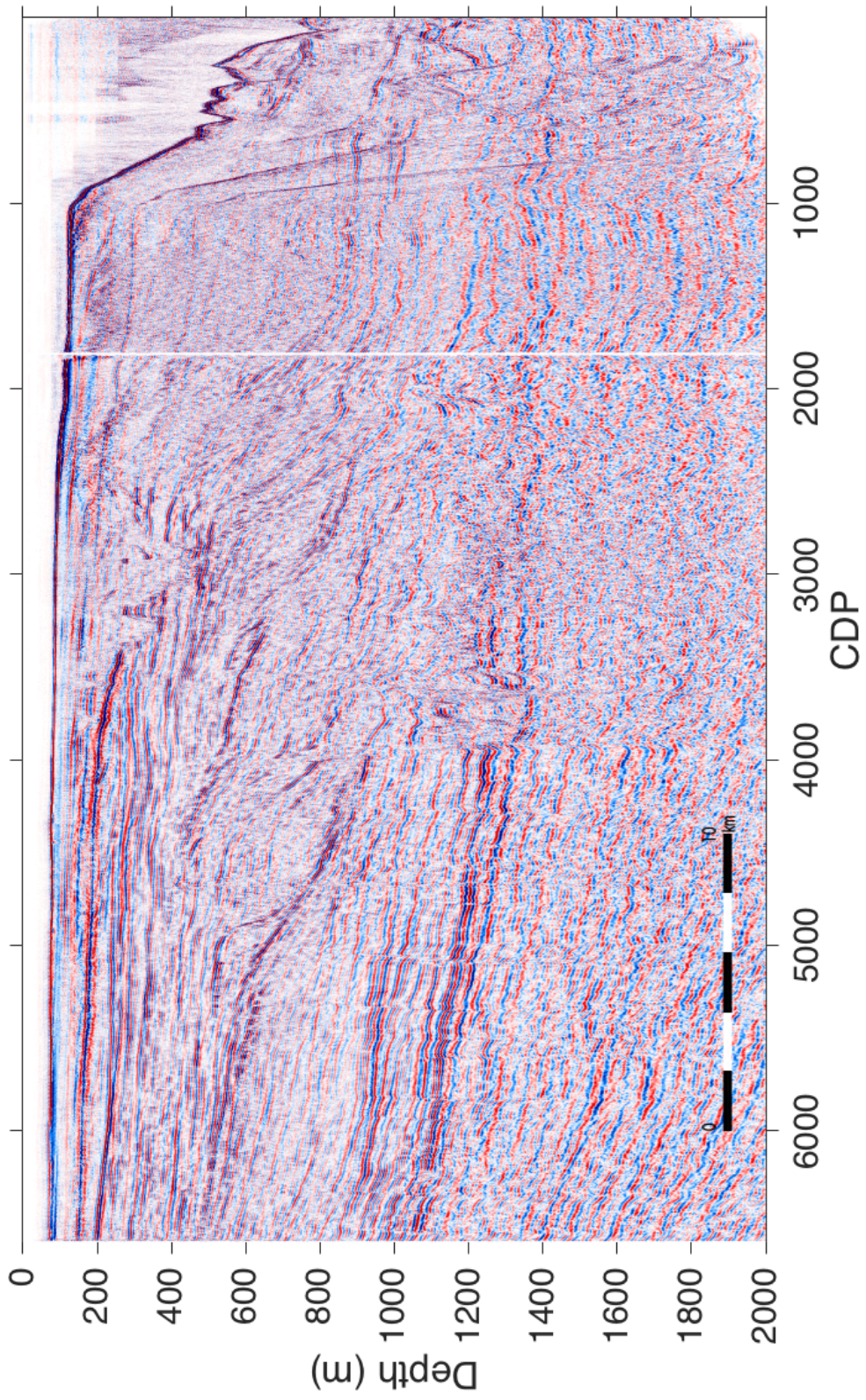

Figure A.1: Stacked image of the depth-migrated section after interval velocity refinement was done by horizon-based tomography.

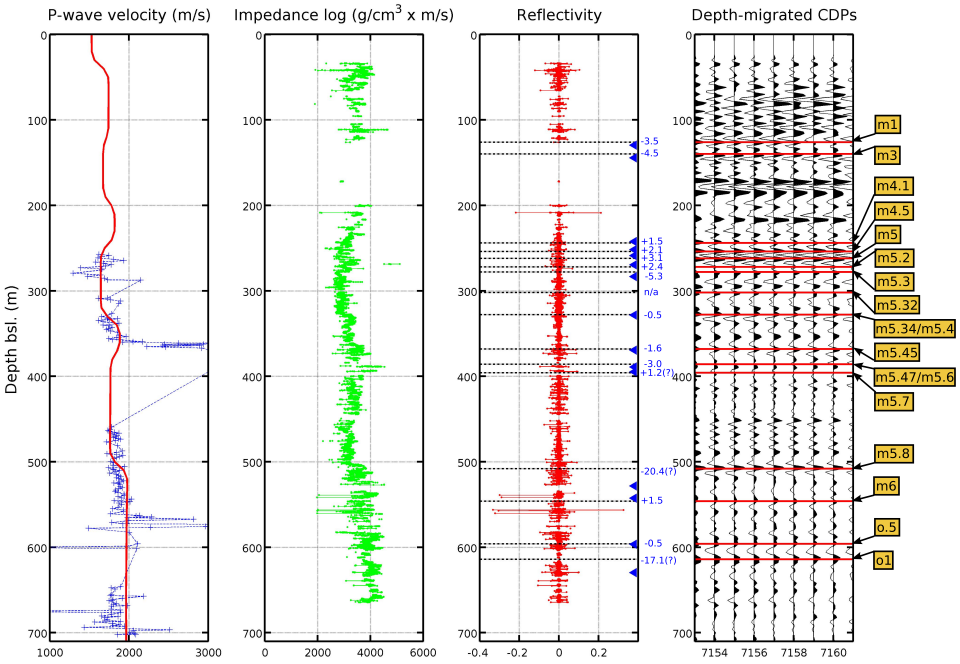

Figure A.2: Correlation between log information from borehole M27, recorded during IODP Leg 313, and the interval velocity model created for Oc270_529 by Riedel et al. (2016a).

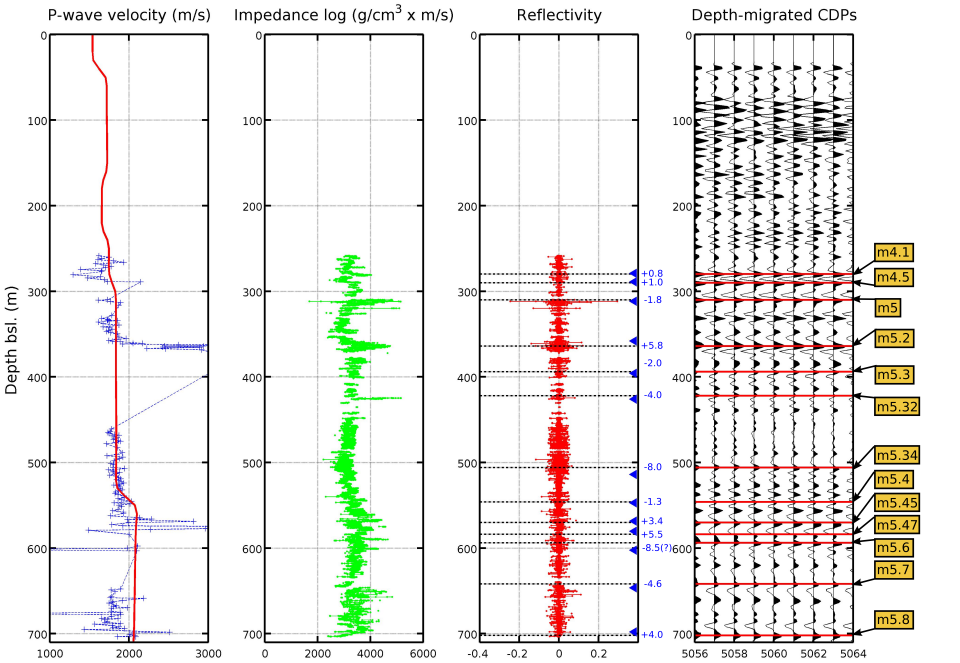

Figure A.3: Correlation between log information from borehole M28, recorded during IODP Leg 313, and the interval velocity model created for Oc270_529 by Riedel et al. (2016a).

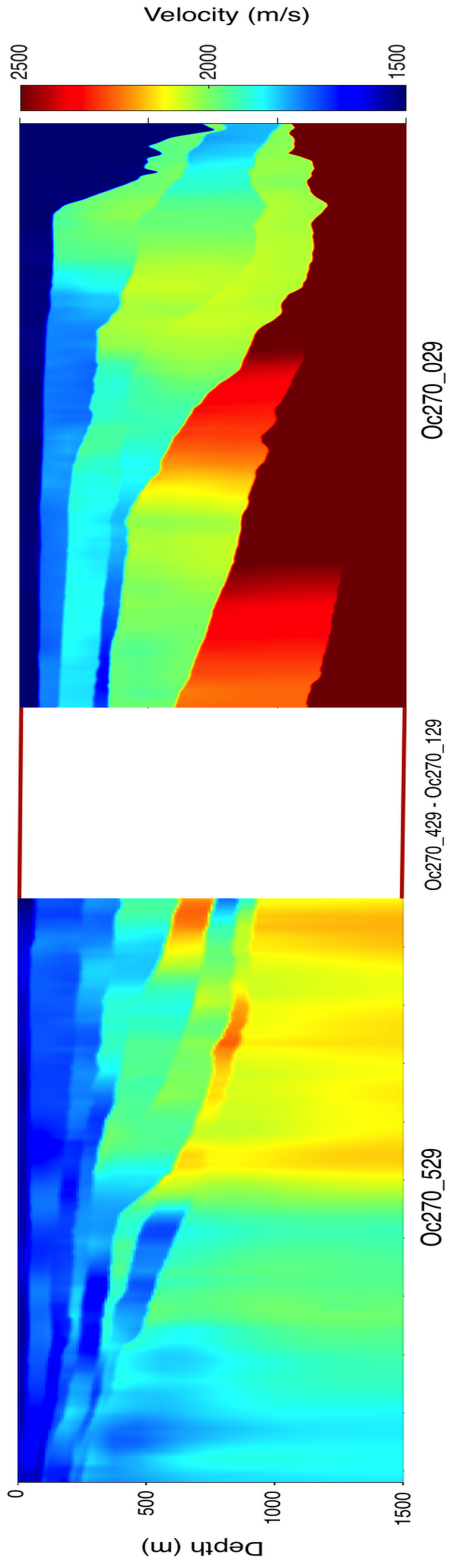

Figure A.4: Combined interval velocity models of seismic profile Oc270_529 and Oc270_029.